bioRxiv preprint doi: https://doi.org/10.1101/2020.12.21.423830; this version posted December 21, 2020. The copyright holder for this preprint (which was not certified by peer review) is the author/funder, who has granted bioRxiv a license to display the preprint in perpetuity. It is made available under aCC-BY-NC-ND 4.0 International license.

Title: Single-cell RNA-sequencing reveals pervasive but highly cell type-specific genetic ancestry effects on the response to viral infection

Authors: Haley E Randolph[1], Zepeng Mu[1], Jessica K Fiege[2,3], Beth K Thielen[4], Jean-Christophe Grenier[5], Mari S Cobb[6], Julie G Hussin[5,7], Yang I Li[6,8], Ryan A Langlois[2,3], Luis B Barreiro[1,6,9]*

Affiliations:

[1] Committee on Genetics, Genomics, and Systems Biology, University of Chicago, Chicago, IL, USA

[2] Center for Immunology, University of Minnesota, Minneapolis, MN, USA

[3] Department of Microbiology and Immunology, University of Minnesota, Minneapolis, MN, USA

[4] Department of Pediatrics, Division of Pediatric Infectious Diseases and Immunology, University of Minnesota, Minneapolis, MN, USA

[5] Research Center, Montreal Heart Institute, Montreal, QC, Canada

[6] Section of Genetic Medicine, Department of Medicine, University of Chicago, Chicago, IL, USA

[7] Faculty of Medicine, Université de Montréal, Montreal, QC, Canada

[8] Department of Human Genetics, University of Chicago, Chicago, IL, USA

[9] Committee on Immunology, University of Chicago, Chicago, IL, USA

*Corresponding author: Barreiro, Luis B (lbarreiro@uchicago.edu)

bioRxiv preprint doi: https://doi.org/10.1101/2020.12.21.423830; this version posted December 21, 2020. The copyright holder for this preprint (which was not certified by peer review) is the author/funder, who has granted bioRxiv a license to display the preprint in perpetuity. It is made available under aCC-BY-NC-ND 4.0 International license.

Abstract: Humans vary in their susceptibility to infectious disease, partly due to variation in the immune response following infection. Here, we used single-cell RNA-sequencing to quantify genetic contributions to this variation in peripheral blood mononuclear cells, focusing specifically on the transcriptional response to influenza infection. We find that monocytes are the most responsive to influenza infection, but that all cell types mount a conserved interferon response, which is stronger in individuals with increased European ancestry. By comparing European American and African American individuals, we show that genetic ancestry effects on expression are common, influencing 29% of genes, but highly cell type-specific. Further, we demonstrate that much of this population-associated expression variation is explained by *cis* expression quantitative trait loci, which are enriched for signatures of recent positive selection. Our findings establish common *cis*-regulatory variants—including those that are differentiated by genetic ancestry—as important determinants of the antiviral immune response.

Keywords: Genetic ancestry, single-cell RNA-sequencing, immune responses, influenza infection, natural selection, expression quantitative trait loci (eQTL)

bioRxiv preprint doi: https://doi.org/10.1101/2020.12.21.423830; this version posted December 21, 2020. The copyright holder for this preprint (which was not certified by peer review) is the author/funder, who has granted bioRxiv a license to display the preprint in perpetuity. It is made available under aCC-BY-NC-ND 4.0 International license.

Introduction

Pathogenic viruses constitute one of the strongest sources of selective pressure in human evolutionary history (Barreiro et al., 2009; Enard and Petrov, 2018; Enard et al., 2016; Fumagalli et al., 2011; Siddle and Quintana-Murci, 2014). Prior to the modern era, however, global pandemics on the scale of the 1918 Spanish influenza or the ongoing SARS-CoV-2 pandemic were probably rare. Due to the restricted potential for long-distance (especially intercontinental) exchange, earlier viral epidemics are thought to have been strongly stratified by geography (Enard and Petrov, 2020). Consequently, although most human genetic variation is shared between populations, differences in viral-mediated selection pressures may have driven divergence in the frequencies of polymorphisms that mediate the viral host response (either because of differences in the viruses that caused epidemic outbreaks or heterogeneity in the timing of epidemic events between populations). If so, the pattern of past epidemic outbreaks may have contributed to variation in viral susceptibility observed within and among modern-day human populations—perhaps interacting with or compounding known health disparities that contribute to substantially higher rates of influenza and COVID-19 hospitalization in Black versus non-Hispanic white Americans (e.g., the Centers for Disease Control and Prevention (CDC) estimates a 79% higher rate of influenza-related hospitalizations for Black versus white Americans: (CDC, 2020)).

Genetics is thought to play an important role in explaining population variation in susceptibility to influenza and other viral pathogens (Albright et al., 2008; Kenney et al., 2017). Supporting this view, a study exploring the impact of regulatory genetic variation on gene expression levels (i.e. expression quantitative trait loci [eQTL] studies) following influenza A virus (IAV) infection of human dendritic cells revealed 121 genetic variants that are significantly associated with the immune response to IAV, including one *cis*-acting variant associated with the interferon regulatory factor 7 gene (*IRF7)* that also acts as a *trans*-regulator responsible for genetic effects on a hub of IRF7-induced antiviral genes (Lee et al., 2014). Variation in the gene expression response to IAV *in vitro* is also correlated with genetic ancestry in monocytes derived

bioRxiv preprint doi: https://doi.org/10.1101/2020.12.21.423830; this version posted December 21, 2020. The copyright holder for this preprint (which was not certified by peer review) is the author/funder, who has granted bioRxiv a license to display the preprint in perpetuity. It is made available under aCC-BY-NC-ND 4.0 International license.

from individuals of African and European descent (Quach et al., 2016).

A major limitation of studies to date, however, is their focus on a single, isolated immune cell type. This approach is blind to genetic effects that act in a cell type-specific manner. Further, it fails to capture critical interactions between the array of immune cell types needed to mount an efficient response to a viral infection. To address these limitations, here, we combine single-cell RNA-sequencing with *in vitro* infection assays of peripheral blood mononuclear cells (PBMCs) with pathogenic influenza A virus. We identify both shared and cell type-specific responses to IAV that are detectable only when gene expression estimates are resolved into individual cell types. We then investigate the degree to which the transcriptional response to IAV is structured by European versus African genetic ancestry and dissect likely genetic contributions to these differences. Finally, we investigate whether variants that are associated with ancestry-related differences are likely to have evolved in response to past selection pressure. Our results show that *cis*-regulatory genetic variation contributes to phenotypic differences in the immune response of modern humans to IAV, including both within and between-population variation. Further, some of these variants—especially those linked to autoimmune risk—carry signatures of recent positive selection, particularly in Europeans, suggesting that at least some present-day autoimmune risk loci were adaptive and conferred a functional benefit during our evolutionary history.

Single-cell profiling of the transcriptional response to influenza infection

We exposed peripheral blood mononuclear cells (PBMCs) sampled from a diverse panel of humans to either a mock treatment (negative control) or to the pandemic H1N1 Cal/04/09 influenza A virus (IAV) strain (multiplicity of infection [MOI] 0.5) (n = 180 samples, comprised of paired mock-exposed and IAV-infected samples from each of 90 individuals). Following 6 hours of exposure, we performed single-cell RNA-sequencing on all samples (Fig. 1A). In total, we captured 255,731 single-cell transcriptomes across all individuals and conditions (n = 235,161 high-quality cells retained after filtering, Table S1). In addition, we collected low-pass whole-

bioRxiv preprint doi: https://doi.org/10.1101/2020.12.21.423830; this version posted December 21, 2020. The copyright holder for this preprint (which was not certified by peer review) is the author/funder, who has granted bioRxiv a license to display the preprint in perpetuity. It is made available under aCC-BY-NC-ND 4.0 International license.

genome sequencing for the same individuals (n = 89), which we used to estimate the proportion of African and European admixture for each individual. Self-identified African American (AA, n = 45) individuals had a modest, although highly variable, percentage of European ancestry (mean = 11%, range = 0 – 43%), while self-identified European American (EA, n = 44) individuals displayed more limited levels of African ancestry (mean = 1%, range = 0 – 23%) (Fig. S1A, Table S1). UMAP clustering revealed eight distinct immune cell types (Fig. 1B), with five major cell clusters corresponding to the five main cell types found in PBMCs, including $CD4^+$ T cells, $CD8^+$ T cells, B cells, natural killer (NK) cells, and monocytes.

We first investigated the overall signature of IAV infection on our samples by collapsing the single-cell gene expression values for each of the five main clusters and for all cells together (i.e. "PBMCs", including the major and minor clusters) into pseudobulk estimates per sample. Principal component analysis (PCA) on the PBMC pseudobulk expression data revealed a strong signature of the IAV infection effect, such that mock- and IAV-infected samples strongly separate on PC1, which explains 43% of the variance in the dataset (Fig. S1B, paired t-test, $p < 1x10^{-10}$). Across the five main clusters and the total PBMC pool, monocytes were by far the most responsive to IAV infection (n = 3,999 differentially expressed (DE) genes [38.4% of those tested] with log2 fold-change > 0.5, FDR < 0.05). All other cell types displayed weaker infection effects (12.4 – 19.7% DE genes) (Fig. 1C, Table S2). In support of a major role for monocytes in the IAV response, gene set enrichment analysis (GSEA) revealed that genes that were more responsive in monocytes compared to all other cell types were strongly enriched for genes involved in viral transcription and monocyte-associated biological pathways, such as monocyte chemotaxis (FDR = $4.6x10^{-4}$) (Fig. 1D, Table S3). Moreover, monocytes exhibited the highest levels of intracellular IAV transcripts (i.e., influenza-derived transcripts generated and processed by infected host cells; > 3-fold increase compared to all other cell types, t-test, all p-values < $1x10^{-10}$ for monocytes compared to all other cell types) (Fig. 1E). This observation shows that monocytes are either the

bioRxiv preprint doi: https://doi.org/10.1101/2020.12.21.423830; this version posted December 21, 2020. The copyright holder for this preprint (which was not certified by peer review) is the author/funder, who has granted bioRxiv a license to display the preprint in perpetuity. It is made available under aCC-BY-NC-ND 4.0 International license.

cell type most susceptible to viral entry, the most permissible to intracellular replication of the virus, or both.

We then explored the extent to which the infection response was concordant or discordant across the five major PBMC cell types. Overall, we found a strong correlation between the response to IAV infection across cell types (Pearson's r range 0.65 – 0.95 across pairwise cell type comparisons, Fig. S1C). However, we also observed many genes for which the response to infection was discordant between cell types. For example, among differentially-expressed genes shared by monocytes and NK cells (n = 822), 138 genes (16.8%, Fig. S1D) responded to IAV infection in the opposite direction (Fig. 1F). To further dissect cell type-specific versus shared responses, we generated a per-gene specificity score based on the coefficient of variation of the log2 fold-change response across cell types for each gene that was significantly differentially-expressed in at least one cell type (high values indicate highly cell type-specific responses to IAV, low values indicate shared responses to IAV) (Table S4). Genes with highly cell type-specific patterns of response were enriched for roles in translational initiation, co-translational protein targeting to membrane, and viral gene expression (FDR < $1x10^{-10}$ for all terms, Fig. 1G, left, Table S4). In contrast, genes with low specificity scores were enriched for pathways related to type I interferon (IFN) signaling (FDR < $1x10^{-10}$) and response to type I IFN (FDR = $7.1x10^{-4}$) (Fig. 1G, right, Table S4). Thus, induction of IFN-related genes appears to be a fundamental component of the antiviral response that is shared across immune cell types (Fig. 1H, top). One notable exception to this observation is the gene *IFNG*, which encodes the type II IFN cytokine IFN-γ. IFN-γ is a crucial mediator of antiviral immunity (Kang et al., 2018), but shows an expression pattern that is almost exclusive to NKT cells in the IAV-infected condition (Fig. 1H, bottom). Collectively, our results underscore the importance of considering the immune responses of single cell types independently. Not only does this approach reveal distinct, cell type-specific responses to viral infection, but also highlights responses that would be undetectable or potentially misleading in more heterogeneous immune cell populations (e.g. PBMCs).

bioRxiv preprint doi: https://doi.org/10.1101/2020.12.21.423830; this version posted December 21, 2020. The copyright holder for this preprint (which was not certified by peer review) is the author/funder, who has granted bioRxiv a license to display the preprint in perpetuity. It is made available under aCC-BY-NC-ND 4.0 International license.

Genetic ancestry is associated with the transcriptional immune response to IAV

We next identified genes for which gene expression levels are correlated with quantitative estimates of genetic ancestry in either the mock condition, the IAV-infected condition, or both (after controlling for age, batch, and other technical covariates). To increase power and improve our effect size estimates for these "population differentially-expressed" (popDE) genes, we implemented a multivariate adaptive shrinkage method (mash) (Urbut et al., 2019), which leverages the correlation structure of genetic ancestry effect sizes across cell types (see Methods for details in the statistical models used). Across conditions and cell types, we identified 1,949 popDE genes (local false sign rate (lfsr) < 0.10), ranging from 830 in NK cells to 1,235 genes in $CD4^+$ T cells (Fig. 2A, Table S5). Within each cell type, most popDE genes were shared between mock and IAV-infected conditions (52.9% in monocytes – 77.4% in $CD8^+$ T cells). In contrast, across cell types, we found that genetic ancestry effects on gene expression were highly cell type-specific, such that the majority of popDE genes were identified in only one or two cell types (52.2% in mock, 51.4% in IAV-infected) (Fig. 2B). For example, *CXCL8*, which encodes IL-8, an important mediator of the inflammatory response (Bickel, 1993), is more highly expressed with increasing African ancestry following IAV infection only in monocytes (lfsr = 0.051 in monocytes and lfsr > 0.25 in all other cell types) (Fig. 2C, top). There are, however, a minority of genes that exhibit shared genetic ancestry effects across all five cell types (17.8% in mock, 24.7% in IAV-infected). One such gene is *IL32*, which encodes a cytokine that induces other proinflammatory cytokines to activate the NF-κB pathway (Ca and Sh, 2006; Yan et al., 2018). *IL32* is more highly expressed with increasing African ancestry in all cell types following infection (lsfr < 8.8×10^{-6}) (Fig. 2C, bottom).

To identify the functional pathways most closely associated with genetic ancestry, we performed enrichment analysis on the popDE effects using the Molecular Signatures Database

bioRxiv preprint doi: https://doi.org/10.1101/2020.12.21.423830; this version posted December 21, 2020. The copyright holder for this preprint (which was not certified by peer review) is the author/funder, who has granted bioRxiv a license to display the preprint in perpetuity. It is made available under aCC-BY-NC-ND 4.0 International license.

hallmark gene sets (Liberzon et al., 2015) (Fig. 2D, Table S6). In monocytes, we identified significant enrichment for multiple immune pathways prior to infection, including the IFN-α response (FDR = 1.9×10^{-3}), IFN-γ response (FDR = 5.4×10^{-4}), TNFα signaling via NF-κB (FDR = 6.1×10^{-4}), IL-2/STAT5 signaling (FDR = 2.1×10^{-3}), and inflammatory response (FDR = 0.012) (Fig. 2D). In all cases, these enrichments were identified for genes that were more highly expressed at baseline (i.e., in the mock treatment condition) in individuals with a greater proportion of African ancestry. Intriguingly, in IAV-infected cells, this pattern shifts: post-infection, we observed enrichment of type I and II IFN pathways (IFN-α response FDR = 0.014, IFN-γ response FDR = 0.040 in monocytes) (Fig. 2D) in genes more highly expressed with increasing European ancestry, as opposed to African ancestry. To better characterize this shift, we constructed a per-individual, per-condition score of interferon signaling activity (termed IFN score) by calculating the average mean-centered expression of genes belonging to the hallmark IFN-α and IFN-γ gene sets (Liberzon et al., 2015). This simple summary statistic revealed that increased European ancestry strongly correlates with increased IFN score, but only in the IAV condition (mean Pearson's r across cell types = -0.26, Fisher's meta-p = 2.9×10^{-6} in the IAV condition, Fisher's meta-p = 0.746 in the mock condition) (Fig. 2E).

These findings suggest that, for some immune pathways (particularly interferon signaling pathways), genetic ancestry may also predict the magnitude of the response to IAV infection. To explicitly test this possibility, we identified significant interactions between treatment condition (mock versus IAV) and genetic ancestry levels. After mash estimation of interaction effect sizes across cell types, we identified 609 genes for which ancestry was associated with the response to infection (i.e., "population differentially-responsive" [popDR] genes, lfsr < 0.10). PopDR genes were found for all five cell types (number of popDR genes range = 84 – 334), but were most common in monocytes (n popDR genes = 334) (Fig. 2F); a core set of 27 popDR genes were also shared across cell types (Fig. S2A, Table S7). In agreement with our previous results, we found that increased European genetic ancestry predicts a stronger type I/II IFN response (measured

bioRxiv preprint doi: https://doi.org/10.1101/2020.12.21.423830; this version posted December 21, 2020. The copyright holder for this preprint (which was not certified by peer review) is the author/funder, who has granted bioRxiv a license to display the preprint in perpetuity. It is made available under aCC-BY-NC-ND 4.0 International license.

as the difference in IFN score between the IAV-infected and mock conditions per individual) across cell types (mean Pearson's r across cell types = -0.23, Fisher's meta-p = $6.x10^{-5}$) (Fig. S2B). This observation cannot be explained by differences in baseline levels of IAV-specific serum IgG antibodies (Figure S2C, S2D). Type I/II IFN response magnitude also correlated with the level of IAV transcripts measured in PBMCs, such that the stronger the IFN response, the higher the measured IAV transcripts (adj. R^2 = 0.553, p = $2.8x10^{-17}$) (Fig. 2G), a relationship primarily driven by monocytes (Fig. S2E). Accordingly, in line with their stronger type I/II IFN response, individuals with increased European ancestry proportion displayed increased levels of IAV transcript expression compared to individuals with higher levels of African ancestry (Pearson's r = -0.32, p = 0.002, Fig. S2F), an observation that is replicated when monocytes are infected with IAV in isolation (O'Neill et al., 2020). These results point to the possibility that ancestry-associated variation in susceptibility to intracellular infection and/or differences in the ability to restrict viral replication may explain ancestry-associated differences in the type I/II IFN response.

Cis-regulatory genetic variation explains ancestry-associated differences in gene regulation

To assess the contribution of genetic variation to genetic ancestry-associated differences in the transcriptional response to IAV infection, we integrated genome-wide expression profiles with genotyping data to map expression quantitative trait loci (eQTL) in both the mock and IAV-infected samples. We focused specifically on *cis*-eQTL, which we defined as SNPs located either within or flanking (±100 kilobases, kb) each gene of interest. We identified 2,234 genes that were associated with at least one *cis*-eQTL (lfsr < 0.10, hereafter referred to as eGenes) across all cell types and conditions tested (Fig. 3A, Table S8). Although many variants exert similar effects across cell types and infection conditions (45%, Fig. S3A), 13 - 24% of the eGenes identified within each cell type were only detected in one condition even after probing patterns of shared

bioRxiv preprint doi: https://doi.org/10.1101/2020.12.21.423830; this version posted December 21, 2020. The copyright holder for this preprint (which was not certified by peer review) is the author/funder, who has granted bioRxiv a license to display the preprint in perpetuity. It is made available under aCC-BY-NC-ND 4.0 International license.

effects using mash (Urbut et al., 2019). Our results thus highlight the importance of gene–environment interactions in influencing transcriptional regulation in the immune system (Barreiro et al., 2012; Fairfax et al., 2014; Lee et al., 2014; Nédélec et al., 2016; Quach et al., 2016). Of note, we identified a set of 29 eGenes (Fig. S3A) that, across all cell types, were only detected in the IAV-infected condition, including the key IFN-inducible genes *OAS1*, *IFI44L*, *IFIT1*, *IRF1*, and *ISG15*. In *OAS1*, the top *cis* SNP across cell types (rs10774671) is an IAV-specific response eQTL (Fig. 3B, top: mock-infected lfsr = 0.81, bottom: IAV-infected lfsr = 1.5×10^{-12} in $CD4^+$ T cells) that lies within a Neanderthal-derived haplotype (Sams et al., 2016) and that has been associated with higher OAS1 enzymatic activity (Bonnevie-Nielsen et al., 2005) and susceptibility to different viruses from the *Flaviviridae* family (El Awady et al., 2011; Kwon et al., 2013; Lim et al., 2009).

We next tested whether eGenes were also likely to be differentially-expressed by genetic ancestry. Across all cell types and conditions, eGenes (lfsr < 0.10) were 3.2 to 6.5-fold more likely to be classified as popDE (lfsr < 0.10) than expected by chance (Fig. 3C). This enrichment suggests that ancestry-associated differences in gene expression are likely to have a substantial genetic component, perhaps due to divergence in allele frequencies at the causal eQTL. To formally evaluate this contribution, we calculated the correlation between 1) the estimated genetic ancestry effect from our popDE analysis, and 2) the predicted genetic ancestry effect based only on the effect size of the top eQTL per eGene and the genotype for this SNP among individuals of European and African ancestry (restricted to those popDE genes that were also eGenes in at least one cell type, n = 835 genes; see Methods for details). We found a striking correlation (Fig. 3D), such that genotype information on the eQTL alone explained an average of 52.5% (mock) and 53.6% (IAV-infected) of the variance in genetic ancestry effect sizes across cell types (Fig. S3B). These results indicate that, among popDE genes with an eQTL, on average, over 50% of the population differences are explained by *cis*-regulatory variation.

bioRxiv preprint doi: https://doi.org/10.1101/2020.12.21.423830; this version posted December 21, 2020. The copyright holder for this preprint (which was not certified by peer review) is the author/funder, who has granted bioRxiv a license to display the preprint in perpetuity. It is made available under aCC-BY-NC-ND 4.0 International license.

Polygenic selection has shaped genetic ancestry-associated differences in ribosomal protein gene expression

We next sought to evaluate if the intersection set of popDE genes and eGenes clustered into specific biological pathways. We identified a strong enrichment for Gene Ontology (GO) terms related to transcriptional and translational processes, including "ribosomal small subunit biogenesis" and "viral transcription" (FDR < $3x10^{-10}$ in mock-infected and IAV-infected) (Fig. 3E), as well as more canonical immune-related pathways, such as myeloid/leukocyte activation and degranulation (Table S9). The observed gene expression divergence between populations in genes linked to similar biological functions could be explained by two hypotheses: 1) genes associated with such biological processes have evolved under relaxed evolutionary constraint, allowing them to accumulate *cis*-regulatory variants that have randomly diverged in allele frequencies via neutral genetic drift, or 2) *cis*-variants regulating these genes have undergone non-neutral shifts in allele frequencies, resulting in the accumulation of alleles that systematically influence the behavior of enriched pathways in a directional manner – a pattern consistent with polygenic selection.

To test for polygenic selection, for each of the enriched pathways, we calculated the median ancestry-associated differential expression effect (i.e., the estimated difference in gene expression between European- and African-ancestry individuals) across all popDE genes contained in a given pathway (limited to those with an eQTL). Under neutrality, we expect the direction of the ancestry-associated effects to be randomly distributed (i.e., some genes will be more highly expressed in European-ancestry individuals whereas others will be more highly expressed in African-ancestry individuals). In contrast, under polygenic selection, we expect to find a directional effect, such that most genes for a given pathway show higher expression in one ancestry group versus the other. Interestingly, most of the GO terms for ribosomal protein-related pathways (e.g. ribosomal biogenesis, viral transcription, etc.) show median population-associated differences in gene expression levels that are consistently higher in individuals with increased

bioRxiv preprint doi: https://doi.org/10.1101/2020.12.21.423830; this version posted December 21, 2020. The copyright holder for this preprint (which was not certified by peer review) is the author/funder, who has granted bioRxiv a license to display the preprint in perpetuity. It is made available under aCC-BY-NC-ND 4.0 International license.

European ancestry across cell types, in both IAV-infected cells (Fig. 3F, 3G) and mock-exposed cells (Fig. S4A). Importantly, these differences are attenuated when regressing out the effects of the associated top *cis*-eQTLs for the genes (Fig. 3F, 3G), suggesting that such differences are driven by the cumulative effect of regulatory variants impacting the expression of ribosomal protein (RP) genes. Strikingly, we found a strong correlation between the average expression of RP eGenes and IAV transcript expression in both $CD8^+$ T cells (Pearson's r = 0.32, p = 0.002) and monocytes (Pearson's r = 0.58, $p < 1x10^{-10}$, Fig. 3H). Together, these data raise the possibility that viral infection-induced selection pressures have shaped ribosomal biology phenotypes in human populations, with potential implications for viral control mechanisms.

Natural selection and susceptibility to autoimmune disease

Past selection imposed by pathogen exposure has been speculated to contribute to present-day susceptibility to autoimmune and chronic inflammatory diseases (Brinkworth and Barreiro, 2014; Sanz et al., 2018). However, it remains unclear whether natural selection has also contributed to genetic ancestry-associated differences in vulnerability to these diseases. To address this question, we performed colocalization analysis between the union set of eQTLs detected across all cell types and conditions and 14 publicly available genome-wide association study (GWAS) hits for 11 autoimmune diseases (Table S10). Colocalized eQTLs are expected to be strongly enriched for causal drivers of variation in disease susceptibility across individuals. Across all autoimmune diseases, we colocalized eQTL in our study with a total of 95 GWAS variants (Fig. 4A, Table S10).

To analyze a broader array of immune-related colocalization signals, we combined our data with colocalization results for bulk eQTLs in 18 immune cell types from 3 large immune eQTL studies (DICE (n = 91) (Schmiedel et al., 2018), DGN (n = 922) (Battle et al., 2014), and BLUEPRINT (n = 197) (Chen et al., 2016)) for the same 14 autoimmune GWAS (Mu et al., 2020). This approach allowed us to identify 1,030 colocalized GWAS hits across the 11 traits (mapping

bioRxiv preprint doi: https://doi.org/10.1101/2020.12.21.423830; this version posted December 21, 2020. The copyright holder for this preprint (which was not certified by peer review) is the author/funder, who has granted bioRxiv a license to display the preprint in perpetuity. It is made available under aCC-BY-NC-ND 4.0 International license.

to 536 eGenes, Table S10). We then asked if these putative causal variants were enriched for signatures of natural selection in the 1000 Genomes Project CEU and YRI populations, using either the integrated haplotype score (iHS, a within-population measure of recent positive selection based on haplotype homozygosity (Voight et al., 2006)) or extreme values of population differentiation (F_{ST}). Far more colocalized loci display high |iHS| scores (values > 95th percentile of the genome-wide distribution) in the CEU population than expected by chance (p = 0.008, Fig. 4B), while no significant enrichment was detected in YRI. Our results thus suggest that natural selection has acted on these *cis*-regulatory autoimmune risk variants, particularly in Europeans, with the caveat that the vast majority of GWAS studies to date have focused exclusively on individuals of European ancestry (Bustamante et al., 2011), preventing us from detecting signatures of selection among GWAS loci unique to African-ancestry individuals. Moreover, we observed that colocalized genes are more likely to be differentially-expressed between populations than expected by chance (35.8% are classified as popDE, p = 0.007) (Fig. 4C), pointing to a potential genetic contribution for the differences in the incidence of autoimmune and inflammatory disorders reported between African and European-ancestry individuals (Brinkworth and Barreiro, 2014).

Within our set of colocalized eGene-SNP pairs, 48 eGenes carried a signature of recent positive selection in either the CEU or YRI populations (|iHS| or F_{ST} > 95th percentile of the genome-wide distribution) (Fig. 4D). Many of these genes involve crucial immune-related functions. For example, the Crohn's disease-susceptibility risk variant rs2284553 colocalized with *IFNGR2,* the gene encoding the beta chain of the IFN-γ receptor, in naïve CD8^{+} T cells (Fig. S5A). This variant is found at much higher frequency in the CEU population (MAF = 0.38) than the YRI population (MAF = 0.05) and shows a signature of recent positive selection in the CEU (iHS = 2.22). Another variant detected in the allergic disease GWAS, rs5743618, maps to a non-synonymous SNP located in *TLR1* that is also an eQTL for the nearby gene *TLR6* (Fig. S5B). This variant compromises NF-κB signaling and activation to produce an attenuated inflammatory

bioRxiv preprint doi: https://doi.org/10.1101/2020.12.21.423830; this version posted December 21, 2020. The copyright holder for this preprint (which was not certified by peer review) is the author/funder, who has granted bioRxiv a license to display the preprint in perpetuity. It is made available under aCC-BY-NC-ND 4.0 International license.

response (Barreiro et al., 2009) and is a known *trans*-regulatory hotspot (Piasecka et al., 2018; Quach et al., 2016). Notably, it is found at low frequency in the YRI population (derived allele frequency (DAF) = 0.04) but is found at elevated frequency in the CEU population (DAF = 0.67) (Sanz et al., 2018). This difference in allele frequency alone explains the positive correlation between African genetic ancestry and the transcriptional response to immune stimulation with antigens that signal through TLR1 (Nédélec et al., 2016; Quach et al., 2016; Sanz et al., 2018).

Discussion

Together, our results provide the most detailed characterization to date of the genetic determinants that shape inter-individual and genetic ancestry-associated differences in the response to viral infection across the five most common immune cell types found in PBMCs. We identified thousands of genes for which expression levels are correlated with genetic ancestry across different immune cell types, but found that the majority of these cases (52.2% in mock, 51.4% in IAV-infected) are restricted to only one or two cell types. These results are likely explained by a combination of cell type-specific genetic effects and environmental factors that correlate with genetic ancestry but that only act on certain cell types. For example, chronic stress has been shown to causally alter immune gene regulation, yet its effects are mainly limited to helper T cells and NK cells (Snyder-Mackler et al., 2016). Although our findings corroborate previous reports of elevated inflammatory pathway activity with increasing African ancestry, at least at baseline (*25*, *26*), they also reveal a novel pattern: increased activity of type I/II IFN pathways following influenza infection associated with increased European ancestry. This observation has potential clinical implications, as interferons are the main defensive cytokines released during the early phase of acute influenza infection as well as most other viral infections. However, when chronically elevated, interferons can increase susceptibility to the uncontrolled inflammation typical of severe cases of influenza and now COVID-19 (Vabret et al., 2020). More studies are now needed to define whether ancestry-associated variation in the interferon

bioRxiv preprint doi: https://doi.org/10.1101/2020.12.21.423830; this version posted December 21, 2020. The copyright holder for this preprint (which was not certified by peer review) is the author/funder, who has granted bioRxiv a license to display the preprint in perpetuity. It is made available under aCC-BY-NC-ND 4.0 International license.

response to viral infection *in vivo* is associated with differential viral clearance, disease severity, and disease outcome.

Many of the genetic ancestry-associated differences in immune regulation we observe are driven by allele frequency differences at *cis*-regulatory variants. Among popDE genes in which we identify at least one *cis*-eQTL across cell types and conditions, we estimate that, on average, *cis*-eQTLs explain approximately 53% of the variance in the observed ancestry-associated differences. This is likely an underestimate, given that it assumes that each gene has only a single *cis*-eQTL, when in fact many genes have been shown to have two or more independent cis-eQTL (Lappalainen et al., 2013). Further, we are underpowered to detect *trans* associations, and we do not consider non-SNP regulatory variants (e.g., indels and copy number variation), which also influence gene expression variation in humans (Gymrek et al., 2016). In addition, we provide evidence for ancestry-associated directional shifts in molecular traits (i.e., gene expression phenotypes related to specific biological pathways) that are under *cis*-regulatory genetic control, highlighting the potential role of polygenic selection in the history of these phenotypes.

The signature of selection at ribosomal protein (RP) genes (*RPL*, *RPS*) is of particular interest, as RPs facilitate translation initiation of viral transcripts (Haque and Mir, 2010; Huang et al., 2012) and directly interact with viral mRNA and proteins to enable viral protein synthesis (Li, 2019). These proteins also play essential roles in ribosomal biogenesis (Fromont-Racine et al., 2003), a process that influences viral reproduction and cell-intrinsic immune responses following human cytomegalovirus infection (Bianco and Mohr, 2019), and that also affects innate immune signaling pathways to modulate the IFN-γ-mediated inflammatory response (Vyas et al., 2009) and NF-κB target gene expression (Wan et al., 2011). Further, a subset of ribosomes, known as immunoribosomes, has been hypothesized to preferentially synthesize antigenically-relevant cellular and viral peptides for immunosurveillance by the MHC class I system, resulting in a tight link between translation and antigen presentation that may allow immune cells to more quickly recognize and eliminate infected cells (Wei and Yewdell, 2019; Yewdell, 2007). Together, these

bioRxiv preprint doi: https://doi.org/10.1101/2020.12.21.423830; this version posted December 21, 2020. The copyright holder for this preprint (which was not certified by peer review) is the author/funder, who has granted bioRxiv a license to display the preprint in perpetuity. It is made available under aCC-BY-NC-ND 4.0 International license.

371 observations support the argument that RPs are important mediators of the host immune
372 response to virus, and raise the possibility that polygenic selection on ribosomal pathways has
373 contributed to present-day variation in viral control within and between human populations.

374 Finally, our results provide evidence that recent, local positive selection has acted on
375 putatively causal regulatory risk variants associated with common autoimmune diseases in
376 GWAS, strengthening the link between pathogen-mediated selection and susceptibility to
377 autoimmune disorders (Brinkworth and Barreiro, 2014; Nielsen et al., 2017; Quach and Quintana-
378 Murci, 2017). The connection between infectious diseases and chronic inflammatory disorders is
379 further supported by reports that some pathogens are contributing, and possibly causal, factors
380 to the development of certain chronic inflammatory and autoimmune diseases (e.g., Epstein–Barr
381 virus and systemic lupus erythematosus, rheumatoid arthritis, and multiple
382 sclerosis; *Mycobacterium avium* and Crohn's disease; *Yersinia enterocolica* and inflammatory
383 bowel disease) (Abubakar et al., 2008; Feller et al., 2007; James et al., 2001; Ramos-Casals et
384 al., 2005; Saebo et al., 2005; Yamazaki et al., 2005). Our findings shed light on human
385 evolutionary history and lend key empirical support to arguments that link historical pathogen-
386 mediated selection to present-day susceptibility to autoimmune and inflammatory diseases.

bioRxiv preprint doi: https://doi.org/10.1101/2020.12.21.423830; this version posted December 21, 2020. The copyright holder for this preprint (which was not certified by peer review) is the author/funder, who has granted bioRxiv a license to display the preprint in perpetuity. It is made available under aCC-BY-NC-ND 4.0 International license.

Acknowledgements: We thank Jenny Tung, Briana Mittleman, Genelle Harrison, and members of the Barreiro lab for their constructive comments and feedback. This work was completed in part with resources provided by the University of Chicago Research Computing Center. Figure 1A was created with BioRender.com.

Funding: This work was supported by grant R01-GM134376 to L.B.B. H.E.R is supported by a National Science Foundation Graduate Research Fellowship (DGE-1746045).

Author contributions: L.B.B directed the study. H.E.R. and L.B.B designed the experiments. J.K.F, B.K.T., and R.A.L. generated the influenza A Cal/04/09 strain used for the infection experiments. H.E.R. performed the *in vitro* PBMC infection experiments. H.E.R. performed the sequencing library preparation, with help from M.S.C. H.E.R. led the computational analyses, with contributions from Z.M., Y.I.L. (colocalization analysis), J.C.G. and J.G.H. (iHS calculations). H.E.R. and L.B.B. wrote the manuscript, with input from all authors.

Declaration of interests: Authors have no competing interests to declare.

bioRxiv preprint doi: https://doi.org/10.1101/2020.12.21.423830; this version posted December 21, 2020. The copyright holder for this preprint (which was not certified by peer review) is the author/funder, who has granted bioRxiv a license to display the preprint in perpetuity. It is made available under aCC-BY-NC-ND 4.0 International license.

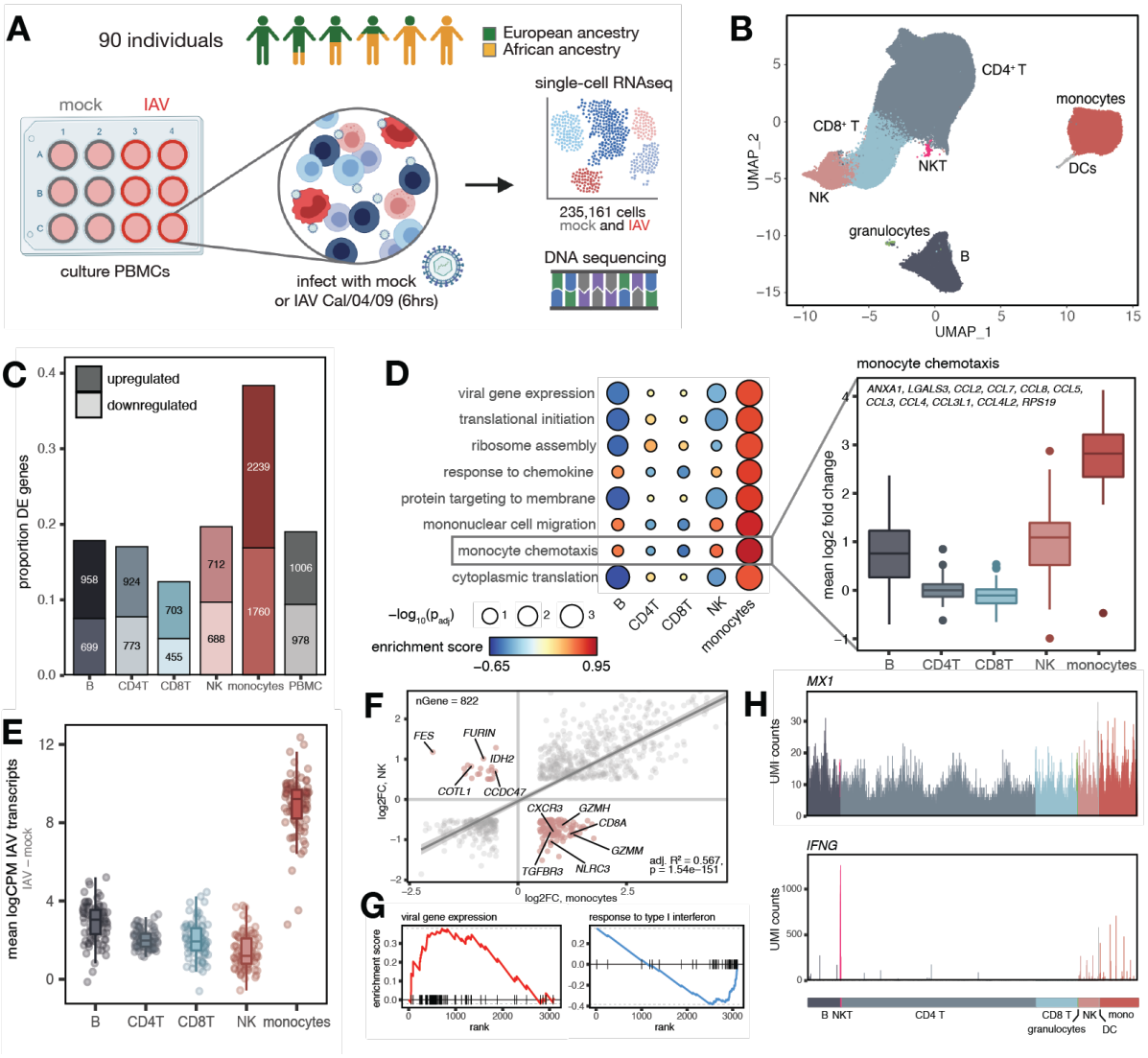

403 **Fig. 1.** Shared and cell type-specific transcriptional responses to IAV infection. (A) Study design
404 schematic. PBMCs from 90 individuals were exposed to mock-conditioned media or IAV
405 Cal/04/09 *in vitro* for 6 hours, followed by single-cell RNA sequencing and DNA collection for DNA
406 sequencing. (B) UMAP of 235,161 high-quality single-cell transcriptomes from both mock- and
407 IAV-infected cells across all individuals. (C) Numbers and proportions of genes that show
408 differential expression (logFC > 0.5, FDR < 0.05) between mock- and IAV-infected conditions
409 across the five major PBMC cell types. (D) Monocyte-specific GO pathways that show significant
410 upregulation (enrichment score > 0, FDR < 0.10) following infection. Genes in the "monocyte
411 chemotaxis" term are significantly more upregulated after IAV infection in monocytes compared

bioRxiv preprint doi: https://doi.org/10.1101/2020.12.21.423830; this version posted December 21, 2020. The copyright holder for this preprint (which was not certified by peer review) is the author/funder, who has granted bioRxiv a license to display the preprint in perpetuity. It is made available under aCC-BY-NC-ND 4.0 International license.

412 to the other cell types (plotted means for each individual across genes in the IAV condition minus
413 the mock condition, t-test, all p-values < $1x10^{-10}$ when comparing monocytes against each other
414 cell type). (E) Distribution of IAV transcript expression across cell types, with monocytes showing
415 a 3 – 6-fold higher number of IAV transcripts compared to any other cell type (t-test, all p-values
416 < $1x10^{-10}$ when comparing monocytes against each other cell type). (F) Correlation between IAV
417 infection effect sizes (log2 fold-change values) in monocytes (x-axis) and NK cells (y-axis) among
418 DE genes in both monocytes and NK cells (n = 822). Line shows the best-fit slope and intercept
419 from a linear model. Highlighted genes (pink) display discordant responses following IAV
420 infection. (G) Example pathways enriched among genes with high (right, viral gene expression
421 FDR = < $1x10^{-10}$) and low (left, response to type I interferon FDR = $7.1x10^{-4}$) specificity scores,
422 where all genes are rank-ordered by specificity score on the x-axis (highest to lowest). (H) UMI
423 counts (y-axis) per cell (x-axis) in the IAV-infected condition for example genes that show
424 ubiquitous expression across cell types (*MX1*, top) and highly cell type-specific expression
425 patterns (*IFNG*, bottom).

bioRxiv preprint doi: https://doi.org/10.1101/2020.12.21.423830; this version posted December 21, 2020. The copyright holder for this preprint (which was not certified by peer review) is the author/funder, who has granted bioRxiv a license to display the preprint in perpetuity. It is made available under aCC-BY-NC-ND 4.0 International license.

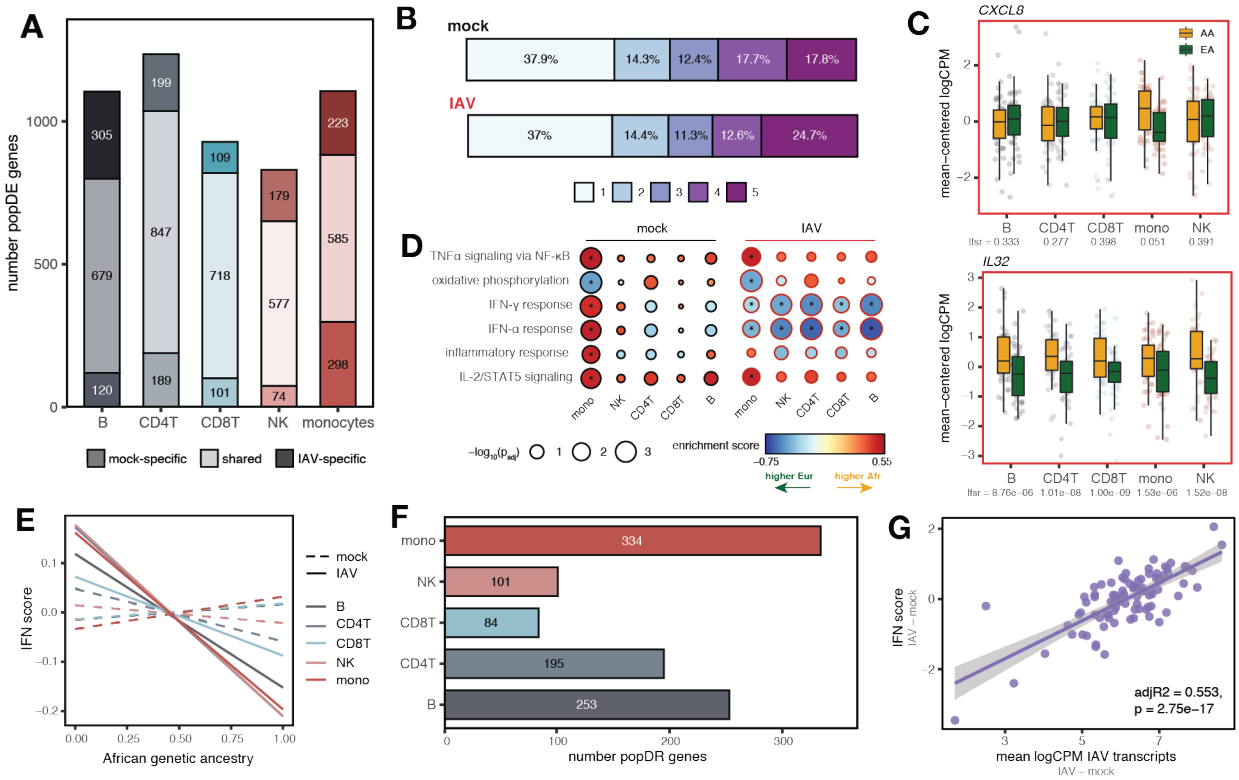

Fig. 2. Genetic ancestry influences the immune response to IAV infection. (A) Number of significant mock-specific, shared, and IAV-specific popDE genes (lfsr < 0.10) across cell types. (B) Cell type sharing of significant popDE effects (1 = popDE effect is detected in only a single cell type, 5 = popDE effect is detected across all cell types). (C) Examples of cell type-specific (*CXCL8*, monocytes lfsr = 0.051, lfsr > 0.25 in all other cell types) and shared (*IL32*, lsfr < 8.8×10^{-6} in all cell types) popDE genes (AA in yellow, EA in green) in the IAV-infected condition. (D) GO enrichments for popDE effects across cell types in the mock-infected (black circles) and the IAV-infected (red circles) conditions. A positive enrichment score (ES) corresponds to an enrichment in genes with higher expression in individuals with increased African ancestry, while a negative ES corresponds to an enrichment in genes with higher expression in individuals with increased European ancestry. * represents pathways with FDR < 0.10. (E) Correlation between the proportion of African genetic ancestry (x-axis) and IFN score (y-axis) in the mock-infected (dotted lines, mean Pearson's r across cell types = -0.0045, Fisher's meta-p = 0.746) and the IAV-

bioRxiv preprint doi: https://doi.org/10.1101/2020.12.21.423830; this version posted December 21, 2020. The copyright holder for this preprint (which was not certified by peer review) is the author/funder, who has granted bioRxiv a license to display the preprint in perpetuity. It is made available under aCC-BY-NC-ND 4.0 International license.

infected condition (solid lines, mean Pearson's r across cell types = -0.26, Fisher's meta-p = 2.9×10^{-6}). (F) Number of significant popDR genes (lfsr < 0.10) across cell types. (G) IAV transcript levels (x-axis) predict the IFN score response (difference in IFN score between the IAV-infected and mock-infected conditions, y-axis) in PBMCs (adj R^2 = 0.553, p = 2.8×10^{-17}), and most individual cell types (Fig. S2C). In (E) and (G), lines show the best-fit slope and intercept from a linear model.

bioRxiv preprint doi: https://doi.org/10.1101/2020.12.21.423830; this version posted December 21, 2020. The copyright holder for this preprint (which was not certified by peer review) is the author/funder, who has granted bioRxiv a license to display the preprint in perpetuity. It is made available under aCC-BY-NC-ND 4.0 International license.

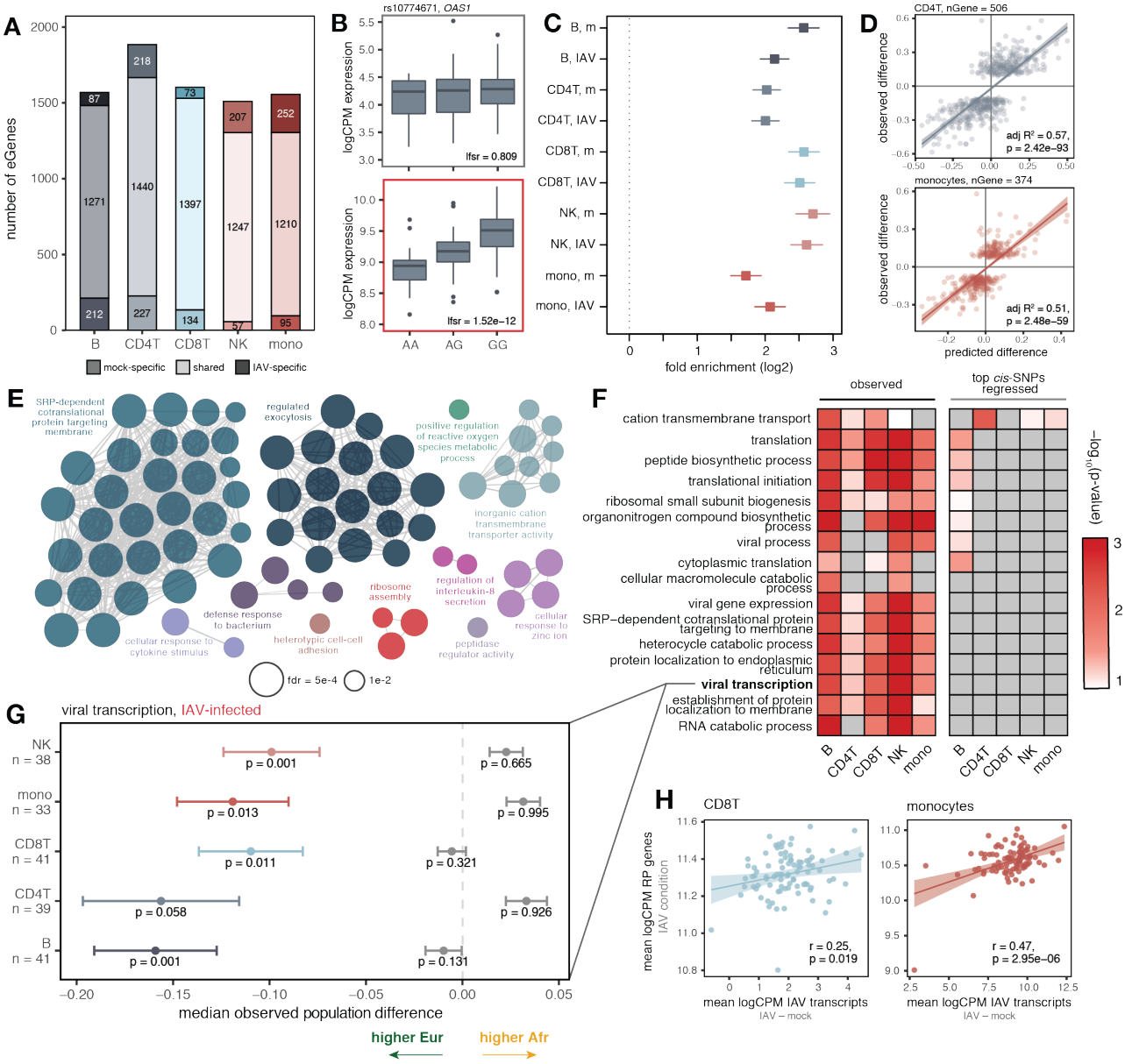

446

447 **Fig. 3.** *Cis*-regulatory variation drives differences in the antiviral response, both at the individual
448 and population levels. (A) Number of significant mock-specific, shared, and IAV-specific eGenes
449 (lfsr < 0.10) across cell types. (B) Example of a condition-specific response eQTL (rs10774671 in
450 *OAS1*) in CD4^{+} T cells (top: mock-infected, lfsr = 0.809, bottom: IAV-infected, lfsr = 1.5x10^{-12}). (C)
451 Enrichment of significant eGenes (lfsr < 0.10) among significant popDE genes (lfsr < 0.10)
452 identified in each cell type and condition (x-axis: log2 fold enrichment with a 95% confidence
453 interval; "m" = mock). (D) Correlation of the *cis*-predicted population differences in expression (x-

bioRxiv preprint doi: https://doi.org/10.1101/2020.12.21.423830; this version posted December 21, 2020. The copyright holder for this preprint (which was not certified by peer review) is the author/funder, who has granted bioRxiv a license to display the preprint in perpetuity. It is made available under aCC-BY-NC-ND 4.0 International license.

axis) versus the observed population differences in expression (y-axis) among popDE genes with an eQTL in $CD4^+$ T cells (top, adj R^2 = 0.57, p = 2.42×10^{-93}) and monocytes (bottom, adj R^2 = 0.51, p = 2.48×10^{-59}). (E) Significant (FDR < 0.01) ClueGO enrichments for the popDE genes that are also eGenes across all cell types in the IAV-infected condition. (F) Median observed population differences among genes in (E) for selected terms using a model estimating the observed genetic ancestry effects (left) and a model estimating this effect with the effect of the top *cis*-SNP regressed for all genes contained in the term (right). (G) Example term showing the effect of *cis* SNP regression. European-ancestry individuals display higher expression (median observed pop. difference < 0, colored point +/- SE) for the genes belonging to the "viral transcription" term in the observed data. Following *cis*-SNP regression (grey point +/- SE), this difference is attenuated. (H) Correlation between IAV transcript levels and the mean logCPM among ribosomal protein (RP) eGenes per individual in the IAV condition minus the mock condition for $CD8^+$T cells (Pearson's r = 0.25, p = 0.019) and monocytes (Pearson's r = 0.47, p = 3×10^{-6}). In (D) and (H), line shows the best-fit slope and intercept from a linear model.

bioRxiv preprint doi: https://doi.org/10.1101/2020.12.21.423830; this version posted December 21, 2020. The copyright holder for this preprint (which was not certified by peer review) is the author/funder, who has granted bioRxiv a license to display the preprint in perpetuity. It is made available under aCC-BY-NC-ND 4.0 International license.

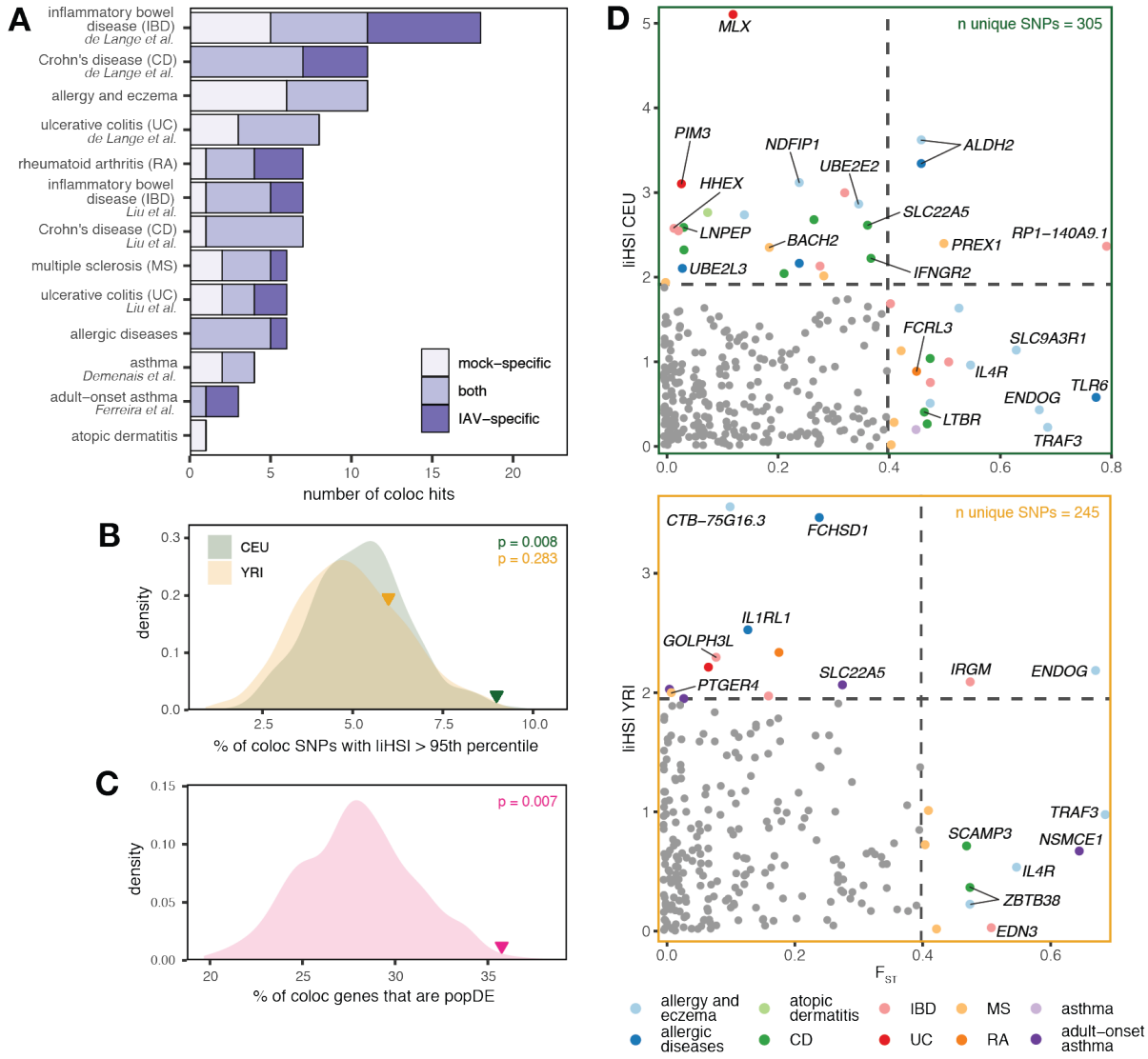

Fig. 4. Recent positive selection has acted on *cis*-regulatory variants implicated in autoimmune disease risk. (A) Number of shared and condition-specific colocalization hits identified across cell types (x-axis) in the 11 autoimmune traits tested (y-axis). (B) Proportion of independent, colocalized lead GWAS loci that have |iHS| values > 95th percentile of the genome-wide distribution among SNPs with > 5% MAF (CEU: green triangle, p = 0.008, YRI: yellow triangle, p = 0.283) compared to random expectation when sampling the same number of SNPs 1,000 times from all variants with a MAF > 5% in an LD-matched and MAF-matched manner (density distributions) among all autoimmune traits. (C) Proportion of genes with a colocalization signal

bioRxiv preprint doi: https://doi.org/10.1101/2020.12.21.423830; this version posted December 21, 2020. The copyright holder for this preprint (which was not certified by peer review) is the author/funder, who has granted bioRxiv a license to display the preprint in perpetuity. It is made available under aCC-BY-NC-ND 4.0 International license.

that are popDE (pink triangle, p = 0.007) compared to random expectation when sampling the same total number of genes 1,000 times from all genes tested (density distribution) among all autoimmune traits. (D) F_{ST} and |iHS| values among the colocalized hits shown in A as well as those identified in the harmonized bulk eQTL data. F_{ST} values are plotted on the x-axis, while |iHS| values are plotted on the y-axis (top: CEU, bottom: YRI). Dotted lines show the 95th percentile of the genome-wide distribution for the respective selection statistic (F_{ST} = 0.398, |iHS| CEU = 1.92, |iHS| YRI = 1.95). eGenes with a selection statistic > 95th percentile are represented by a colored point, and colors represent the autoimmune trait for which a colocalization signal is detected (here, the multiple inflammatory bowel disease, ulcerative colitis, and Crohn's disease GWAS have been collapsed into a single label).

bioRxiv preprint doi: https://doi.org/10.1101/2020.12.21.423830; this version posted December 21, 2020. The copyright holder for this preprint (which was not certified by peer review) is the author/funder, who has granted bioRxiv a license to display the preprint in perpetuity. It is made available under aCC-BY-NC-ND 4.0 International license.

Methods

Peripheral blood mononuclear cell (PBMC) collections

All samples were obtained from BioIVT. A signed, written consent was obtained from each participant. Blood was collected from 90 male donors between the ages of 21 – 69 who identified as either African-American (AA) (n = 45) or European-American (EA) (n = 45) from the same collection site in Miami, Florida (United States) utilizing a standard protocol with a sodium heparin anticoagulant. Briefly, PBMCs were extracted from whole blood using a density gradient, washed with HBSS, reconstituted in CryoStor CS10 to a concentration of 10 million (M) cells/ml, and subsequently cryopreserved. Between 6 – 10M cells per individual were frozen per vial. We decided to only focus on males to avoid the potentially confounding effects of sex-specific transcriptional differences in the response to infection. Only individuals self-reported as currently healthy were included in the study. All individuals had detectable levels of IAV-specific serum IgG antibodies, but no differences in antibody titers were identified between European and African-ancestry individuals (Figure S2C, S2D).

Generation of influenza A virus

Influenza A virus California/04/2009 (Cal/04/09) virus was rescued in 293T cells by plasmid-based transfection with IAV Cal/04/09 in the pDZ vector using methods previously described (Fodor et al., 1999; Hai et al., 2010; Hoffmann et al., 2000). 24 hours following transfection, 7.5×10^5 MDCK cells were added to the culture in Opti-MEM containing TPCK trypsin (1 μg/mL). For the following two days, 500 μL of Opti-MEM containing TPCK trypsin (2 μg/mL) was added to the culture. One day later, the supernatant was harvested, centrifuged to remove cellular debris, and stored at -80°C. Cal/04/09 was amplified on MDCK cells to generate a stock. Uninfected MDCK cells were cultured for 48 – 72 hours and supernatant was harvested to generate the control, mock-conditioned media. Stocks were plaqued on MDCK cells. Cells were infected in infection media (PBS with 10% Ca/Mg, 1% penicillin/streptomycin, 5% BSA) at 37°C

bioRxiv preprint doi: https://doi.org/10.1101/2020.12.21.423830; this version posted December 21, 2020. The copyright holder for this preprint (which was not certified by peer review) is the author/funder, who has granted bioRxiv a license to display the preprint in perpetuity. It is made available under aCC-BY-NC-ND 4.0 International license.

for 1 hour. Infection media was replaced with an agar overlay (2X MEM, 1 μg/mL TPCK trypsin, 1% DEAE-dextran, 5% $NaCo_3$, 2% oxoid agar), and cells were cultured at 37°C for 40 hours then fixed with 4% formaldehyde. Blocking and immunostaining were done for 1 hour at 25°C in 5% milk. Primary stain was mouse anti-Cal/04/09 (1:5000), secondary stain was peroxidase sheep anti-mouse-HRP (1:5000) (45001275, GE Healthcare). TrueBlue Peroxidase Substrate (50-647-28, Kirkegard & Perry Laboratories) was used as directed for detection of virus plaques.

In vitro infection experiments and sample collections

PBMCs were unfrozen approximately 14 hours prior to infection and cultured overnight in RPMI 1640 supplemented with 10% fetal bovine serum (FBS), 2 mM L-glutamine, and 10 ug/ml gentamycin. Infection experiments were performed over 15 batches, where each experimental batch was semi-balanced for self-identified ancestry label to avoid introducing a batch effect confounded with genetic ancestry. The morning of the experiment, 1M PBMCs were plated at a concentration of 1M/ml for each condition, and exposed to either mock-conditioned media (negative control) or Cal/04/09 IAV at an MOI of 0.5. After 30 minutes of exposure, the control media or virus was washed from PBMC cultures, cells were replated, and cells were then incubated for 6 hours at 37°C in 5% CO_2 and 20% O_2. Following the 6 hour incubation, cells were collected, washed, and prepared for single-cell capture using the 10X workflow. Immediately prior to the capture, cells from samples were combined into two pools (6 samples per pool) each balanced for infection status (mock-infected and IAV-infected) and genetic ancestry (Table S1). Multiplexed cell pools were used as input for the single-cell captures, and for each cell pool, 10,000 cells were targeted for collection using the Chromium Single Cell 3' Reagent (v2 chemistry) kit (10X Genomics). Post Gel Bead-in-Emulsion (GEM) generation, the reverse transcription (RT) reaction was performed in a thermal cycler as described (53°C for 45 min, 85°C for 5 min), and post-RT products were stored at -20°C until downstream processing (no longer

bioRxiv preprint doi: https://doi.org/10.1101/2020.12.21.423830; this version posted December 21, 2020. The copyright holder for this preprint (which was not certified by peer review) is the author/funder, who has granted bioRxiv a license to display the preprint in perpetuity. It is made available under aCC-BY-NC-ND 4.0 International license.

than 4 days post-RT reaction). For DNA processing, 1M PBMCs were collected, and DNA was extracted using the DNeasy Blood and Tissue Kit (Qiagen) following the “Cultured cells” protocol.

Single-cell library preparation and RNA-sequencing

Post-RT reaction cleanup, cDNA amplification, and sequencing library preparation were performed as described in the Single Cell 3’ Reagent Kits v2 User Guide (10X Genomics). Briefly, cDNA was cleaned with DynaBeads MyOne SILANE beads (ThermoFisher Scientific) and amplified in a thermal cycler using the following program: 98°C for 3 min, 11 cycles x 98°C for 15 s, 67°C for 20 s, 72°C for 1 min, and 72°C 1 min. After cleanup with the SPRIselect reagent kit (Beckman Coulter), the libraries were constructed by performing the following steps: fragmentation, end-repair, A-tailing, SPRIselect cleanup, adaptor ligation, SPRIselect cleanup, sample index PCR (98°C for 45 s, 14 cycles x 98°C for 20 s, 54°C for 30 s, 72°C for 20 s, and 72°C 1 min), and SPRIselect size selection. Batches of four experiments (corresponding to eight multiplexed single-cell captures) were processed at a time. Prior to sequencing, all multiplexed single-cell libraries (n = 30) were quantified using the KAPA Library Quantification Kit for Illumina Platforms (Roche) and pooled in an equimolar ratio. Libraries were sequenced 100 base pair paired-end (R1: 30 cycles, I1: 10 cycles, R2: 85 cycles) on an Illumina NovaSeq to an average depth of 45,612 mean reads per cell across all batches (average median genes detected per cell across batches = 689).

Low-pass DNA sequencing and VCF processing

Out of the 90 individuals in the cohort, 89 were successfully genotyped using DNBseq low-pass whole-genome sequencing (BGI) at 4x coverage. Variants were called across individuals using the human reference genome (GRCh37), yielding a merged VCF, and the ImputeSeq low-pass imputation pipeline (Gencove) was used to perform VCF imputation. The imputed merged VCF was lifted over to GRCh38 with CrossMap (v0.3.9) (Zhao et al., 2014) using

bioRxiv preprint doi: https://doi.org/10.1101/2020.12.21.423830; this version posted December 21, 2020. The copyright holder for this preprint (which was not certified by peer review) is the author/funder, who has granted bioRxiv a license to display the preprint in perpetuity. It is made available under aCC-BY-NC-ND 4.0 International license.

564 the GRCh37 to GRCh38 Ensembl chain file downloaded at
565 ftp://ftp.ensembl.org/pub/assembly_mapping/homo_sapiens/ and the GRCh38 FASTA file from
566 ftp://ftp.ensembl.org/pub/release-92/fasta/homo_sapiens/dna/. For each individual, low-quality
567 variants were filtered by only retaining those with a maximum genotype probability (GP in
568 FORMAT field) > 0.90 using QCTOOL (v2.0.7, https://www.well.ox.ac.uk/~gav/qctool_v2/). If the
569 max(GP) for a variant was < 0.90, the variant call was automatically set to missing. Only
570 autosomal, biallelic SNPs were kept for downstream analysis using the SelectVariants function (-
571 -select-type-to-include SNP) from GATK (v3.7).
572
573 Estimation of genome-wide admixture levels
574 Prior to estimation of genome-wide admixture proportions, samples were merged with
575 CEU (n = 99, Utah Residents [CEPH] with Northern and Western European Ancestry) and YRI (n
576 = 108, Yoruba in Ibadan, Nigeria) samples from the 1000 Genomes Project (1000GP) Phase 3
577 dataset (Auton et al., 2015) (downloaded from
578 ftp://ftp.1000genomes.ebi.ac.uk/vol1/ftp/release/20130502/supporting/GRCh38_positions/). The
579 proportion of European and African genetic ancestry for each individual included in the study was
580 estimated using the supervised clustering algorithm in ADMIXTURE (v1.3.0) (Alexander and
581 Lange, 2011). A total of 13,518,147 unlinked SNPs (r^2 between all pairs < 0.1) were used for
582 genetic ancestry assignments, assuming k = 2 ancestral clusters. These estimated quantitative
583 genetic ancestry proportions were used to assess differences in immune responses between
584 populations.
585
586 Mapping, demultiplexing, and initial cell filtering
587 FASTQ files from each multiplexed capture library were mapped to a custom reference
588 containing GRCh38 and the Cal/04/09 IAV reference genome (downloaded from NCBI, created
589 using cellranger mkref) using the cellranger (v3.0.2) (10X Genomics) count function. souporcell

bioRxiv preprint doi: https://doi.org/10.1101/2020.12.21.423830; this version posted December 21, 2020. The copyright holder for this preprint (which was not certified by peer review) is the author/funder, who has granted bioRxiv a license to display the preprint in perpetuity. It is made available under aCC-BY-NC-ND 4.0 International license.

(v2.0, Singularity v3.4.0) (Heaton et al., 2020) in --skip_remap mode (-k 6) was used to demultiplex cells into samples based on genotypes from a common variants file (1000GP samples filtered to SNPs with >= 2% allele frequency in the population, downloaded from https://github.com/wheaton5/souporcell). Briefly, souporcell clusters cells based on cell allele counts in common variants, assigning all cells with similar allele counts to a single cluster corresponding to one individual, while also estimating singlet/doublet/negative status for that cell. For each batch, hierarchical clustering of the true genotypes known for each individual (obtained from low-pass whole-genome-sequencing) and the cluster genotypes estimated from souporcell was used to assign individual IDs to souporcell cell clusters. All 89 individuals were successfully assigned to a single cluster.

After demultiplexing cells into samples, Seurat (v3.1.5, R v3.6.3) (Stuart et al., 2019) was used to perform quality control filtering of cells. In total, we captured 255,731 cells prior to filtering (range of cells recovered per capture: min. = 5534, max. = 10805). Cells were considered "high-quality" and retained for downstream analysis if they had: 1) a "singlet" status called by souporcell, 2) between 200 – 2500 genes detected (nFeature_RNA), and 3) a mitochondrial reads percentage < 10%, leaving 236,993 cells (n = 19,248 genes).

Clustering, cell type assignment, and UMAP analysis

We performed two versions of clustering analysis and cell type assignment: 1) in which IAV genes were kept in the raw count matrix (used as input for pseudobulk calculations), and 2) in which IAV genes were subset out of the raw count matrix (for visualization of the UMAP in Fig. 1B). All other steps of the clustering workflow (implemented in Seurat v3.1.5) remained the same. Pseudobulk expression estimates (see below) between clustering versions for cell type-matched clusters were extremely similar (adj R^2 > 0.999 for comparisons between versions). For both clustering iterations, we split the cells by infection status (mock or IAV) and ran SCTransform to normalize and scale the UMI counts within condition. In this step, we simultaneously regressed

bioRxiv preprint doi: https://doi.org/10.1101/2020.12.21.423830; this version posted December 21, 2020. The copyright holder for this preprint (which was not certified by peer review) is the author/funder, who has granted bioRxiv a license to display the preprint in perpetuity. It is made available under aCC-BY-NC-ND 4.0 International license.

out variables corresponding to experiment batch and percent mitochondrial reads per cell. The data was then integrated on infection status using the SelectIntegrationFeatures, PrepSCTIntegration, FindIntegrationAnchors, and IntegrateData workflow. Following integration, dimensionality reduction was performed via UMAP (RunUMAP function, dims = 1:30) and PCA (RunPCA function, npcs = 30). A Shared Nearest Neighbor (SNN) Graph was constructed using the FindNeighbors function (dims = 1:20, all other parameters set to default), and clusters were subsequently called using the FindClusters algorithm (resolution = 0.5, all other parameters set to default).

Clusters were annotated based on the expression of canonical immune cell marker genes (CD4$^+$ T: *CD3D*$^+$, *CD3E*$^+$, *CD8A*$^-$; CD8$^+$ T: *CD3D*$^+$, *CD8A*$^+$; NK cells: *CD3D*$^-$, *NKG7*$^+$, *GNLY*$^+$; monocytes: *CD14*$^+$, *LYZ*$^+$; B: *MS4A1*$^+$; granulocytes: *PRSS57*$^+$; dendritic cells (DCs): *HLA-DRA*$^+$, *HLA-DRB1*$^+$, *CCR7*$^+$, *CST3*$^+$, *CD83*$^+$). A small group of cells, which were identified as B cells, clustered with CD4$^+$ T cells in the UMAP (Fig. 1B), and we investigated this further to see whether this subset represented a distinct, rare cell type. Further analysis revealed that these cells express markers typical of NKT cells, including *CD3D*, *NKG7*, *IL2*, *TNF*, and *IFNG*, and thus, these cells were manually annotated as NKT cells. In the UMAP constructed from input data containing IAV genes, we excluded 1,832 cells for which we could not confidently assign a cell type, as they clustered on the basis of high IAV transcript expression, leaving us with 235,161 cells across all individuals and conditions for downstream analysis (n CD4$^+$ T cells = 138,801, CD8$^+$ T cells = 32,446, monocytes = 27,020, B cells = 22,877, NK cells = 13,220, DCs = 374, granulocytes = 301, NKT cells = 122).

Calculation of pseudobulk estimates

Cluster-specific pseudobulk estimates were used to summarize single-cell expression values into bulk-like expression estimates within samples (where, here, a sample is an individual, infection-condition pair, n = 180). This was performed for all five major cell types (CD4$^+$ T cells,

bioRxiv preprint doi: https://doi.org/10.1101/2020.12.21.423830; this version posted December 21, 2020. The copyright holder for this preprint (which was not certified by peer review) is the author/funder, who has granted bioRxiv a license to display the preprint in perpetuity. It is made available under aCC-BY-NC-ND 4.0 International license.

642 CD8$^+$ T cells, B cells, monocytes, NK cells) and PBMCs, where all high-quality cells from all cell
643 types identified (n = 235,161) were treated as a single aggregate cluster. Within each cluster for
644 each sample, raw UMI counts were summed across all cells assigned to that sample for each
645 gene using the sparse_Sums function in textTinyR (v1.1.3), yielding an n x m expression matrix,
646 where n is the number of samples included in the study (n = 180) and m is the number of genes
647 detected in the single-cell analysis (m = 19,248) for each of the 6 clusters.
648
649 Calculation of capture-corrected expression for downstream modeling
650 From this point forward, pseudobulk estimates were treated as de facto bulk expression
651 data for each cell type considered. As such, calculations of residuals and downstream modeling
652 of infection and genetic ancestry effects (see below) were performed for each cluster
653 independently. For each cell type, lowly-expressed genes were filtered using cell-type specific
654 cutoffs (removed genes with a median logCPM < 1.5 in CD4$^+$ T cells, monocytes, and PBMCs, <
655 2.5 in B cells and CD8$^+$ T cells, and < 4.0 in NK cells), leaving the following number of genes per
656 cell type: CD4$^+$ T cells = 9,291, CD8$^+$ T cells = 9,960, B cells = 9,335, monocytes = 10,424, NK
657 cells = 7,109, and PBMCs = 10,430.
658 After removing lowly-expressed genes, normalization factors to scale the raw library sizes
659 were calculated using calcNormFactors in edgeR (v 3.26.8) (Robinson et al., 2010). The voom
660 function in limma (v3.40.6) (Ritchie et al., 2015) was used to apply these size factors, estimate
661 the mean-variance relationship, and convert raw pseudocounts to logCPM values. A model
662 evaluating the technical effect of capture (~ 0 + capture, where capture corresponds to a factor
663 variable representing the 30 experimental capture batches) on gene expression was fit using the
664 lmFit and eBayes functions, and model residuals were obtained using the residuals.MArrayLM
665 function in limma. The average capture effect was then computed by taking the mean of the
666 capture coefficients across all 30 capture batches per gene, and this average capture effect was
667 added back to the residuals across samples to generate the capture-corrected expression

bioRxiv preprint doi: https://doi.org/10.1101/2020.12.21.423830; this version posted December 21, 2020. The copyright holder for this preprint (which was not certified by peer review) is the author/funder, who has granted bioRxiv a license to display the preprint in perpetuity. It is made available under aCC-BY-NC-ND 4.0 International license.

estimates. The inverse variance weights calculated by voom were obtained and included in the respective lmFit call for all downstream models unless otherwise noted.

While performing quality control checks on our data, we noticed that the density distributions of the capture-corrected expression estimates were bimodal for some samples in certain cell types. We estimated this bimodality proportion in each cell type for each sample by: i) estimating the local minimum of the density distribution, ii) subsetting the x-axis on a restricted range that was specific to each cell type, iii) using the x value where y equals the estimated local minimum as the bimodal threshold, and iv) calculating the proportion of genes less than this threshold. Assigned bimodality proportions were manually checked and corrected to an approximate value if they were obviously over- or under-estimated. The bimodality proportion is negatively correlated with cell counts per sample in most cell types and was most pronounced in the $CD8^+$ T cells, monocytes, and NK cells (i.e. the cell types with the fewest number of cells collected per sample). To remove any potentially confounding effects associated with this artifact, the appropriate cell-type specific bimodality proportion vector across samples was included as a quantitative technical covariate in all of our downstream models.

Modeling global infection effects

To obtain estimates of the global infection effects, capture-corrected expression levels of samples corresponding to the same individual were compared in a paired design, in which individuals were introduced as additional covariates into the following differential infection effect model that was run per cell type:

$$\mathrm{M}_1\colon E(i,j) \sim \begin{cases} \beta_0(i,j) + \beta_{pB}(i) \cdot pB^{mock}(j) + \beta_{age}(i) \cdot age(j) + \varepsilon^{mock}(i,j) & \text{if Condition} = mock \\ \beta_0(i,j) + \beta_{IAV}(i) + \beta_{pB}(i) \cdot pB^{IAV}(j) + \beta_{age}(i) \cdot age(j) + \varepsilon^{IAV}(i,j) & \text{if Condition} = IAV \end{cases}$$

Here, $E(i,j)$ represents the capture-corrected expression estimate of gene i for individual j and $\beta_0(i,j)$ represents the intercept corresponding to gene i and individual j (i.e. the expectation of

bioRxiv preprint doi: https://doi.org/10.1101/2020.12.21.423830; this version posted December 21, 2020. The copyright holder for this preprint (which was not certified by peer review) is the author/funder, who has granted bioRxiv a license to display the preprint in perpetuity. It is made available under aCC-BY-NC-ND 4.0 International license.

gene *i*'s expression level in the mock-infected sample for individual *j*). When evaluated, this model gives the global estimate of the IAV infection effect per gene, $\beta_{IAV}(i)$, approximated using the within-individual variation in gene expression across conditions. Further, pB^{cdt} represents the bimodal proportion estimated per sample for the respective cell type being modeled (where *cdt* represents either the mock or IAV), with β_{pB} being the corresponding effect on gene expression, and age represents the mean-centered, scaled (mean = 0, sd = 1) age in years per individual, with β_{age}being the impact of age on expression. Finally, ε^{cdt} represents the residuals for each respective condition (mock or IAV) for each gene *i*, individual *j* pair. Of note, when modeling the expression estimates in PBMCs, two additional covariates were added to the model, corresponding to the first two principal components of a PCA performed on an n x m cell type proportion matrix (where n = number of samples = 180, m = number of cell types = 10, with the matrix populated by the cell type proportions for each sample [calculated by the number of cells per cell type cluster for a sample divided by the total number of cells assigned to that sample]) to account for the majority of the variance introduced by underlying cell type composition (PC1 percent variance explained (PVE) = 53.8%, PC2 PVE = 23.2%, total = 77.0%).

These models were fit using the lmFit and eBayes functions in limma (Ritchie et al., 2015), and the estimates of the global infection effect $\beta_{IAV}(i)$ (i.e. the differential expression effects due to IAV infection) were extracted across all genes along with their corresponding p-values. We controlled for false discovery rates (FDR) using an approach analogous to that of Storey and Tibshirani (Nédélec et al., 2016; Storey and Tibshirani, 2003), which makes no explicit assumptions regarding the distribution of the null model but instead derives it empirically. To obtain a null, we performed 10 permutations, where infection status label (mock/IAV) was permuted within individual. We consider genes significantly differentially-expressed upon infection if they have a β_{IAV} |logFC| > 0.5 and an FDR < 0.05.

bioRxiv preprint doi: https://doi.org/10.1101/2020.12.21.423830; this version posted December 21, 2020. The copyright holder for this preprint (which was not certified by peer review) is the author/funder, who has granted bioRxiv a license to display the preprint in perpetuity. It is made available under aCC-BY-NC-ND 4.0 International license.

717 Calculation of IFN score

718 To construct the IFN score metric, we summarized the expression patterns of genes involved in
719 the type I/II IFN response as a whole, where, within condition, we i) subset on genes belonging
720 to the hallmark IFN gamma and alpha response pathways, ii) mean-centered and scaled the
721 expression values for each gene across individuals, and iii) computed the average scaled
722 expression across genes per individual.

723

724 Modeling genetic ancestry effects and integration with mashr

725 Prior to modeling genetic ancestry effects, capture-corrected expression estimates were
726 quantile-normalized within condition using qqnorm in R. The following nested linear model was
727 used to identify genes for which expression levels are correlated with the proportion of African
728 ancestry across individuals within condition (i.e. popDE genes):

729 $$\text{M}_2\text{: } E(i,j) \sim \begin{cases} \beta_0(i) + \beta_{AA}^{mock}(i) \cdot AA(j) + \beta_{pB}(i) \cdot pB^{mock}(j) + \beta_{age}(i) \cdot age(j) + \varepsilon^{mock}(i,j) \text{ if Condition = } mock \\ \beta_0(i) + \beta_{IAV}(i) + \beta_{AA}^{IAV}(i) \cdot AA(j) + \beta_{pB}(i) \cdot pB^{IAV}(j) + \beta_{age}(i) \cdot age(j) + \varepsilon^{IAV}(i,j) \text{ if Condition = } IAV \end{cases}$$

730 Here, $E(i,j)$ represents the capture-corrected expression estimate of gene i for individual j, $\beta_0(i)$ is
731 the global intercept accounting for the expected expression of gene i in a 100% European-
732 ancestry mock-infected individual, $\beta_{AA}^{mock}(i)$ and $\beta_{AA}^{IAV}(i)$ indicate the effects of African admixture
733 (mean-centered, scaled African ancestry proportion, $AA(j)$) on gene i within each condition, and
734 $\beta_{IAV}(i)$ represents the intrinsic infection effect of IAV infection. All other terms in the model are
735 analogous to that described in M_1. Again, the model was fit using limma, and the estimates $\beta_{AA}^{mock}(i)$
736 and $\beta_{AA}^{IAV}(i)$ of the genetic ancestry effects were extracted across all genes, along with their
737 corresponding p-values. Each of these estimates represents the genetic ancestry-related
738 differential expression effects within each condition.

739 Genes for which the response to IAV infection is correlated with the proportion of African
740 ancestry (i.e. popDR genes) were detected using the following model:

bioRxiv preprint doi: https://doi.org/10.1101/2020.12.21.423830; this version posted December 21, 2020. The copyright holder for this preprint (which was not certified by peer review) is the author/funder, who has granted bioRxiv a license to display the preprint in perpetuity. It is made available under aCC-BY-NC-ND 4.0 International license.

$$M_3: E(i,j) \sim \begin{cases} \beta_0(i,j) + \beta_{pB}(i) \cdot pB^{mock}(j) + \beta_{age}(i) \cdot age(j) + \varepsilon^{mock}(i,j) \text{ if Condition = } mock \\ \beta_0(i,j) + \beta_{IAV}(i) + \beta_{AA}^{IAV}(i) \cdot AA(j) + \beta_{pB}(i) \cdot pB^{IAV}(j) + \beta_{age}(i) \cdot age(j) + \varepsilon^{IAV}(i,j) \text{ if Condition = } IAV \end{cases}$$

This model is similar to M_1 (differential effect of IAV infection), in that it allows us to obtain estimates based on within-individual variability, with the difference that the IAV infection effect is no longer built in a genetic ancestry-independent manner as in model M_1, since it is now dependent on genetic ancestry as follows: $\beta_{IAV} + \beta_{AA}^{IAV}(i) \cdot AA$. In this context, β_{AA}^{IAV} denotes the genetic ancestry-infection interaction effect induced by IAV infection, which represents variation in the response to infection that is correlated with the proportion of African ancestry.

To assess sharing of genetic ancestry effects across cell types and to increase our power to detect these effects, we applied Multivariate Adaptive Shrinkage in R (mashr v0.2.28) (Urbut et al., 2019) to the outputs of our popDE and popDR cell type-by-cell type models. mashr was applied independently to both the popDE and popDR priors, so all following methods were performed twice, once for the popDE effects and then again for the popDR effects. Effect size priors were obtained directly from limma and merged into matrices including all effect sizes across cell types, only keeping those genes detected in all cell types (i.e. n x m matrices, where for popDE effects: n = 6,847 genes, m = 10 conditions [mock- and IAV-infected popDE effects for each of the 5 main cell types], and for popDR effects: n = 6,847 genes, m = 5 conditions [popDR effects for each of the 5 main cell types]). Standard errors of the effect size priors were calculated per gene by multiplying the square root of the posterior variance (s2.post) of each gene by the unscaled standard deviation for the effect size of interest for that gene (stdev.unscaled) estimated by limma, and these values were similarly formatted into matrices as described above. To account for correlations among measurements across conditions in our data, we used the estimate_null_correlation_simple function implemented in mashr to specify a correlation matrix prior to fitting the mash model. We included both the canonical covariance matrices provided by default in mashr and data-driven covariance matrices (defined as the top 5 PCs from a PCA performed on the significant (lfsr < 0.05) signals detected in the condition-by-condition model

bioRxiv preprint doi: https://doi.org/10.1101/2020.12.21.423830; this version posted December 21, 2020. The copyright holder for this preprint (which was not certified by peer review) is the author/funder, who has granted bioRxiv a license to display the preprint in perpetuity. It is made available under aCC-BY-NC-ND 4.0 International license.

results) learned from our data in the mash model fit. For both popDE and popDR effects, the mash model was fit to all tests using the mash function. Posterior summaries of the effect sizes, standard deviations, and measures of significance were extracted. We used the estimated local false sign rate (lfsr) to assess significance of our posterior popDE and popDR effects and considered genes significantly population differentially-expressed or differentially-responsive if the lfsr of the posterior mean was < 0.10.

eQTL mapping and integration with mashr

eQTL mapping was performed independently in each cell type against the sets of genes retained after lowly-expressed gene filtering (n genes: $CD4^+$ T cells = 9,291, $CD8^+$ T cells = 9,960, B cells = 9,335, monocytes = 10,424, NK cells = 7,109, PBMCs = 10,430). A linear regression model was used to examine associations between SNP genotypes and expression levels, in which expression levels were regressed against genotype. Input expression matrices were quantile-normalized within condition prior to running the association. Mock-exposed and IAV-infected eQTL were mapped separately across all cell types. All regressions were performed using the R package MatrixEQTL (v2.3) (Shabalin, 2012). Only SNPs with a minor allele frequency > 5% across all individuals were tested, and SNPs with > 10% of missing data or deviating from Hardy-Weinberg equilibrium at $p < 10^{-5}$ were excluded (--maf 0.05 --geno 0.10 --hwe 0.00001 PLINK v1.9 filters, www.cog-genomics.org/plink/1.9/) (Chang et al., 2015). In total, 6,305,923 SNPs passed our quality-control filters. Local associations (i.e. putative *cis*-eQTL) were tested against all SNPs located within the gene body or 100kb upstream and downstream of the transcription start site (TSS) and transcription end site (TES) for each gene tested. We recorded the minimum p-value (i.e. the strongest association) observed for each gene, which we used as statistical evidence for the presence of at least one eQTL for that gene. To estimate an FDR, we permuted the genotype data ten times, re-performed the linear regressions, and recorded the minimum p-values for the gene for each permutation. These sets of minimum p-values were used

bioRxiv preprint doi: https://doi.org/10.1101/2020.12.21.423830; this version posted December 21, 2020. The copyright holder for this preprint (which was not certified by peer review) is the author/funder, who has granted bioRxiv a license to display the preprint in perpetuity. It is made available under aCC-BY-NC-ND 4.0 International license.

as an empirical null distribution and FDRs were calculated using the method described in the section “Modeling global infection effects”.

Power to detect *cis*-eQTL can be increased by accounting for unmeasured surrogate confounders. To identify these confounders, we first performed PCA on a correlation matrix based on gene expression for mock and IAV-infected samples. Subsequently, up to 20 principal components (PCs) were regressed out prior to performing the association analysis for each gene. A specific number of PCs to regress in each condition and cell type, corresponding to the number of PCs that empirically led to the detection of the largest number of eQTL in each condition, was then chosen from these results. The exact number of PCs regressed in each of the analyses can be found in Table S11. Of note, while PC corrections increase our power to detect eQTL, they do not affect the underlying structure of the expression data.

Mapping was performed combining both EA and AA individuals to increase power. To avoid spurious associations resulting from population structure, the first two eigenvectors obtained from a PCA on the genotype data using SNPRelate (v1.20.1, gdsfmt v1.22.0) (Zheng et al., 2012) were included in the Matrix eQTL model as well. Other covariates included in the linear model were the following: the condition and cell type-specific bimodal proportion and age (mean-centered, scaled), with two additional covariates included when mapping eQTL using the PBMC expression data, corresponding to the first 2 PCs from the cell type composition PCA described in “Modeling global infection effects”.

Our ability to detect eQTL was highly dependent on the number of cells identified in each cell type cluster (correlation between the total number of cells recovered per cell type across all individuals/conditions versus the number of significant eQTL (FDR < 0.10) detected: adj R^2 = 0.983, p = $1x10^{-8}$). To gain power to detect *cis*-eQTL effects using sharing information across cell types, we again implemented mashr (Urbut et al., 2019). Out of necessity of the method, we only considered shared genes that were tested across all cell types (n = 6,573). For each of these genes, we chose a single, top *cis*-SNP, defined as the SNP with the lowest FDR across all cell

bioRxiv preprint doi: https://doi.org/10.1101/2020.12.21.423830; this version posted December 21, 2020. The copyright holder for this preprint (which was not certified by peer review) is the author/funder, who has granted bioRxiv a license to display the preprint in perpetuity. It is made available under aCC-BY-NC-ND 4.0 International license.

types (n = 5) and conditions (n = 2), to input into mashr, yielding a total of 6,573 gene-SNP pairs. We extracted the prior effect sizes (betas) and computed the standard errors (SEs) of these betas (defined as the beta divided by the t-statistic) from the Matrix eQTL outputs for each gene-SNP pair across cell types and conditions. We defined a set of "strong" tests (i.e. the 6,573 top gene-SNP associations) as well as a set of random tests, including both null and non-null tests, which we obtained from randomly sampling 200,000 rows of a matrix containing all gene-SNP pairs tested by Matrix eQTL merged across conditions. Our mashr workflow was as follows: i) the correlation structure among the null tests was learned using the random test subset, ii) the data-driven covariance matrices were learned using the strong test subset, iii) the mash model was fit to the random test subset using canonical and data-driven covariance matrices, with two additional "infection" covariance matrices (i.e. one matrix capturing shared effects in only the mock-exposed samples and another matrix capturing shared effects in only the IAV-infected samples), and iv) the posterior summaries were computed for the strong test subset. We used the estimated local false sign rate (lfsr) to assess significance of our posterior eQTL effects and considered a gene-SNP pair to have a significant eQTL effect if the lfsr of the posterior mean was < 0.10, which we defined as an eGene.

Identification of condition-specific popDE genes and eGenes

Within each cell type, we considered either popDE genes or eGenes as condition-specific (i.e. only showing an effect in either the mock or IAV infection condition) if they had an lfsr < 0.10 in only one condition. Here, we assume that the risk of identifying a true effect in both mock and IAV-infected cells (i.e. a shared popDE gene/eGene) as falsely condition-specific due to lack of power is low, specifically because we employed the multivariate adaptive shrinkage framework, which draws information across conditions to make better-informed posterior estimates about the sharing of effects, so we do not expect to see many posterior effects called as "condition-specific" when, in fact, they are not.

bioRxiv preprint doi: https://doi.org/10.1101/2020.12.21.423830; this version posted December 21, 2020. The copyright holder for this preprint (which was not certified by peer review) is the author/funder, who has granted bioRxiv a license to display the preprint in perpetuity. It is made available under aCC-BY-NC-ND 4.0 International license.

844

845 Enrichment of eGenes within popDE genes

846 We tested for an enrichment of eGenes among the genes identified as popDE genes
847 within each cell type and condition. For each cell type, condition pair, we created two vectors: i)
848 a popDE gene vector, where significant popDE genes (lfsr < 0.1) were coded as a 1 and non-
849 significant popDE genes were coded as a 0, and ii) an eGene vector, where significant eGenes
850 (lfsr < 0.10) were coded as a 1 and non-significant eGenes were coded as a 0. The logistic
851 regression was performed on the popDE gene and eGene vectors using glm in R, where the
852 eGene vector was used as the predictor variable and the popDE gene vector was used as the
853 response variable (popDE[0,1] ~ eGene[0,1]). The odds ratios output by glm were converted to
854 log2 fold enrichments with a 95% confidence interval (plotted along the x-axis in Fig. 3C).

855

856 Calculation of predicted and observed population differences in expression

857 We estimated the predicted *cis*-genetic population differences in gene expression using a
858 method in which we first computed the predicted expression of each gene considering only the
859 posterior effect size of the top *cis* SNP for that gene and an individual's genotype dosage (a vector
860 of 0, 1, or 2), where, for gene *i,* individual *j*:

861 $$predicted\ expression_i = eQTL\ effect\ size_i * genotype_j$$

862 We then modeled these predicted expression values using a model analogous to that of M_2
863 (model evaluating the popDE effects, "Modeling genetic ancestry effects and integration with
864 mashr") to obtain the predicted genetic ancestry effects (plotted on the x-axis for genetically-
865 driven popDE genes in Fig. 3D). The observed population differences in expression were taken
866 directly from the post-mash beta estimates of M_2 (plotted on the y-axis for genetically-driven
867 popDE genes in Fig. 3D).

868

bioRxiv preprint doi: https://doi.org/10.1101/2020.12.21.423830; this version posted December 21, 2020. The copyright holder for this preprint (which was not certified by peer review) is the author/funder, who has granted bioRxiv a license to display the preprint in perpetuity. It is made available under aCC-BY-NC-ND 4.0 International license.

Modeling the effect of *cis*-regression on the observed population differences in expression

To assess the impact of *cis*-regression on population-associated expression differences, we used two models evaluating the effect of continuous genetic ancestry (African ancestry proportion) on gene expression: i) a model analogous to M_2 (model evaluating the popDE effects, "Modeling genetic ancestry effects and integration with mashr"), and ii) a model in which, for each gene, the top *cis* SNP for that gene was regressed by including the genotype dosage for that SNP across individuals as a covariate in the model. The models were fit using limma and mashr was applied (as described in the section "Modeling genetic ancestry effects and integration with mashr") to the prior effect sizes and standard errors derived from both models. The mashr posterior summaries were used to directly obtain the observed population differences in expression for each gene.

For each significantly enriched GO term (FDR < 0.01) identified in Fig. 3E (see "Enrichment analyses" section below), we calculated summaries of the observed population difference in expression among the genes that belong to each term that are also popDE genes with evidence of an eQTL in at least one cell type. To do this, for each cell type for each term, we collected the observed population differences among these term-specific genetically-driven popDE genes and calculated the median and standard error (SE) for these values (plotted on the x-axis in Fig. 3G). This was performed for both the observed ("real") model outputs (model i) as well as the *cis*-regressed model outputs (model ii). For each cell type, we obtained a p-value for the real effects using a permutation method. To obtain a null distribution, we performed 1,000 permutations where, for each iteration, we: 1) sampled the same number of observed term-specific, genetically-driven popDE genes for that cell type from a background set of all genetically-driven popDE for that cell type, 2) obtained the population differences in expression among these genes, and 3) calculated the median for these null values. We then computed a one-sided, empirical p-value, where we considered the number of instances more extreme in the median null difference compared to the median observed difference in the real data given the sign of this

bioRxiv preprint doi: https://doi.org/10.1101/2020.12.21.423830; this version posted December 21, 2020. The copyright holder for this preprint (which was not certified by peer review) is the author/funder, who has granted bioRxiv a license to display the preprint in perpetuity. It is made available under aCC-BY-NC-ND 4.0 International license.

895 difference (i.e. if the observed difference in the real data was < 0, we counted the number of
896 observations in the null distribution equal to or less than the observed value, and if the observed
897 difference in the real data was > 0, we counted the number of observations in the null distribution
898 equal to or greater than the observed value), where p = number of instances more extreme divided
899 by the number of permutations (n = 1000). Similarly, we obtained a p-value for the *cis*-regressed
900 effects using the same method, except for that in steps 2 and 3, we considered the *cis*-regressed
901 population differences as opposed to those seen in the real data. Notably, to calculate the
902 directional p-value for the *cis*-regressed case, we used the magnitude of the median *cis*-regressed
903 population difference but still considered the sign of the median observed population difference.
904
905 Colocalization analysis
906 Specifically for the colocalization analysis, eQTL were remapped in each cell type with
907 Matrix eQTL (Shabalin, 2012) using a 1 megabase (Mb) *cis*-window, with all other modeling
908 parameters kept constant, to broaden our search space and increase our probability of detecting
909 colocalized variants. We assessed colocalization between our identified eQTLs in each cell type,
910 condition pair and 14 publicly-available GWAS summary statistics for 11 autoimmune diseases
911 (Table S10) as previously described (Mu et al., 2020) with a few modifications. Briefly, for each
912 trait, we identified the lead GWAS SNPs with p-values below $1x10^{-5}$ and defined a “locus” as a
913 1Mb window centered around the lead GWAS SNP. Of note, the HLA region (chr6: 25Mb-35Mb)
914 was removed from the analysis. eGenes were defined as those with an lfsr < 0.10 from the mashr
915 posteriors. The coloc.signals function from the coloc (v4.0.4) package in R was used to evaluate
916 colocalization with default priors (Giambartolomei et al., 2014; Wallace, 2020). A colocalization
917 test was only performed if the most significant SNP of an eGene fell within a GWAS locus. We
918 defined colocalization as (PP3+PP4) > 0.5 and PP4/(PP3+PP4) > 0.8, where PP3 corresponds
919 to the posterior probability of having two independent signals (one for the eQTL and one for the

bioRxiv preprint doi: https://doi.org/10.1101/2020.12.21.423830; this version posted December 21, 2020. The copyright holder for this preprint (which was not certified by peer review) is the author/funder, who has granted bioRxiv a license to display the preprint in perpetuity. It is made available under aCC-BY-NC-ND 4.0 International license.

GWAS) and PP4 corresponds to the posterior probability of colocalization between the eQTL and GWAS signals.

To expand the number of colocalized genes considered for downstream analyses, we also downloaded colocalization results between harmonized bulk eQTLs in 18 immune cell types from 3 studies (DICE, DGN, and BLUEPRINT) and the same 14 autoimmune GWAS. To obtain a list of unique colocalized eGene-locus pairs, we merged colocalization results from all 18 immune cell types for each GWAS and only kept the colocalization test with the largest PP4 value for each eGene at each GWAS locus.

Calculation of selection statistics

iHS and F_{ST} values were calculated using the 1000GP Phase 3 dataset (Auton et al., 2015) in the GRCh37/hg19 build (downloaded from ftp://ftp.1000genomes.ebi.ac.uk/vol1/ftp/release/20130502/).

iHS

Prior to calculation, the 1000GP Phase 3 data was filtered to exclude INDELs and CNVs. Ancestral alleles were retrieved from the 6 primates EPO pipeline (version e59) (Herrero et al., 2016), and filtered 1000GP VCF files were converted to change the reference allele to the ancestral allele using bcftools (v1.9) (Li, 2011) with the fixref plugin. The program hapbin (v.1.3.0) (Maclean et al., 2015) was then used to calculate iHS values for the CEU and YRI populations using population-specific genetic maps constructed on the 1000GP OMNI dataset (ftp://ftp.1000genomes.ebi.ac.uk/vol1/ftp/technical/working/20130507_omni_recombination_rates). All downstream analyses used the standardized iHS values reported from hapbin.

F_{ST}

Prior to calculation, the 1000GP Phase 3 data was filtered to keep only biallelic SNPs. F_{ST} statistics were computed between the CEU and YRI populations using the vcftools (v0.1) (Danecek et al., 2011) flag --weir-fst-pop, where the 1000GP CEU samples were defined as

bioRxiv preprint doi: https://doi.org/10.1101/2020.12.21.423830; this version posted December 21, 2020. The copyright holder for this preprint (which was not certified by peer review) is the author/funder, who has granted bioRxiv a license to display the preprint in perpetuity. It is made available under aCC-BY-NC-ND 4.0 International license.

946 population 1 and the YRI samples were defined as population 2. This method is analogous to that
947 described in Weir and Cockerham's 1984 paper (Weir and Cockerham, 1984).
948
949 Enrichment of colocalized hits with popDE genes and iHS statistics
950 *With popDE genes*
951 We tested for an enrichment of popDE genes among genes with a colocalization signal
952 across the 14 autoimmune traits included in the colocalization analysis in aggregate. Considering
953 all colocalized signals, we collected a list of the unique genes associated with colocalization hits,
954 corresponding to the eGenes driving the eQTL signature. Among these genes, we calculated the
955 proportion that are also identified as popDE genes (here, a gene is considered popDE if it is called
956 as significantly (lfsr < 0.10) popDE in at least one cell type and condition) and consider this our
957 "observed proportion". To obtain a null distribution, we performed 1,000 permutations where, for
958 each iteration, we: i) sampled the same number of unique genes associated with colocalization
959 hits from a list of all genes tested for the eQTL analysis that were shared across cell types (n =
960 6205), and ii) calculated the proportion of these genes that are also popDE (our "null percentage").
961 We calculated a p-value by evaluating the number of permutations in which the null percentage
962 was greater than or equal to the observed percentage divided by the number of total permutations
963 (n = 1,000).
964 *With iHS statistics*
965 We then tested for an enrichment of variants with high iHS values (defined as those with
966 an |standardized iHS| > 95th percentile of the genome-wide distribution among our tested SNPs
967 for the population being considered) among colocalized SNPs for all of the autoimmune traits as
968 a group. For both the 95th percentile iHS calculations and our null distribution sampling approach
969 described below, we only considered SNPs that were tested for an eQTL association in Matrix
970 eQTL (i.e. those with a minor allele frequency > 0.05). The 95th percentile |standardized iHS|
971 cutoffs were as follows: CEU = 1.92 and YRI = 1.95. For each tested SNP, we obtained

bioRxiv preprint doi: https://doi.org/10.1101/2020.12.21.423830; this version posted December 21, 2020. The copyright holder for this preprint (which was not certified by peer review) is the author/funder, who has granted bioRxiv a license to display the preprint in perpetuity. It is made available under aCC-BY-NC-ND 4.0 International license.

population-specific allele frequencies calculated from the 1000GP CEU or YRI individuals using the vcftools (v0.1) (Danecek et al., 2011) --freq flag. These alleles frequencies were converted to minor allele frequencies (MAFs) (i.e. if the allele frequency for a SNP was > 0.5, we subtracted it from 1), and SNPs were subsequently partitioned into 5% MAF bins (e.g. bin 1 = 0 – 5% MAF, bin 2 = 5 – 10% MAF, etc. with the rightmost interval closed).

Among the unique colocalized SNPs we identified across traits, we noticed that a subset appeared to be in high linkage disequilibrium (LD) with one another, suggesting that these SNPs likely did not represent independent colocalization signals. To account for this, we systemically identified SNPs with squared inter-variant allele count correlations (r^2) > 0.8 using PLINK (v1.9, --r2 --ld-window-r2 0.8) (Chang et al., 2015) among all the colocalized hits with multiple tag SNPs for a single eGene. To obtain a list of independent colocalized SNPs, we included: 1) those identified as unlinked loci, and 2) only the SNP with the highest |iHS| value among each set of SNPs with an r^2 > 0.8. We then calculated the proportion of those with an |iHS| > 95th percentile and considered this our "observed percentage". To obtain a null distribution, we used a sampling approach that mimicked both the MAF distribution and the underlying LD structure of our true data. We performed 1,000 permutations, where, for each iteration, we treated the sampling for the "independent" and "linked" SNPs separately. To create a null distribution for the "independent" SNPs, we sampled the same number of independent SNPs observed in the real data from the set of all tested SNPs in a MAF bin-matched manner, e.g. if there were 10 colocalized SNPs in MAF bin 3 in the observed data, we sampled 10 SNPs from the set of tested SNPs in MAF bin 3. To obtain a null distribution for the "linked" SNPs, we simulated the underlying LD structure of these variants where, for each eGene in the observed data with multiple tag SNPs (i.e. those SNPs with an r^2 > 0.8), we: i) counted the number of tag SNPs for that gene and obtained the corresponding MAF bin for the SNP with the highest |iHS| value, ii) randomly sampled a set of SNPs from chromosome 1 with r^2 > 0.8 from the MAF bin identified in i), where the number of SNPs in the set was equal to the number of tag SNPs in the observed data, and iii) picked the SNP with the

bioRxiv preprint doi: https://doi.org/10.1101/2020.12.21.423830; this version posted December 21, 2020. The copyright holder for this preprint (which was not certified by peer review) is the author/funder, who has granted bioRxiv a license to display the preprint in perpetuity. It is made available under aCC-BY-NC-ND 4.0 International license.

998 highest |iHS| value among this SNP set. We then combined our simulated independent and linked
999 SNPs and calculated the proportion of those SNPs with an |iHS| > 95th percentile and considered
1000 this our "null percentage". To calculate a p-value, we evaluated the number of permutations in
1001 which the null percentage was greater than or equal to the observed percentage divided by the
1002 number of total permutations (n = 1,000). All of the above analyses were performed twice, once
1003 with iHS values calculated within the CEU population and again with values within the YRI
1004 population.
1005
1006 Enrichment analyses
1007 Gene set enrichment analysis was performed using three independent methods, including
1008 fgsea (Korotkevich et al., 2019), GOrilla (Eden et al., 2009), and ClueGO (Bindea et al., 2009),
1009 depending on the type of data being evaluated. The enrichment program specifications and the
1010 data in which they were used to assess enrichments in are described below:
1011 The R package fgsea (v1.10.1) was used to perform gene set enrichment analysis for the
1012 global infection effects (Fig. 1D) using the C5 gene ontology (GO) biological processes gene sets
1013 and for the popDE effects (Fig. 2D) using the H hallmark gene sets (Subramanian et al., 2005).
1014 For the infection effects, t-statistics were obtained directly from the topTable function in limma,
1015 and for the popDE effects, t-statistics were calculated from the posterior mashr outputs, where
1016 the t-statistic = posterior effect size divided by the posterior standard error for each gene. The t-
1017 statistics were then ranked, and these pre-ranked t-statistics were used to perform the enrichment
1018 using fgsea (Korotkevich et al., 2019) with the following parameters: minSize = 15, maxSize =
1019 500, nperm = 100000. Enrichments scores (ES) and Benjamini-Hochberg adjusted p-values
1020 output by fgsea were collected for each condition and are reported in Fig. 1D and Fig. 2D for the
1021 infection effects and popDE effects, respectively.
1022 We also used fgsea to generate the barcode plots shown in Fig. 1G to visualize where the
1023 genes in the highlighted pathways are found in the ranked specificity score list among the set of

bioRxiv preprint doi: https://doi.org/10.1101/2020.12.21.423830; this version posted December 21, 2020. The copyright holder for this preprint (which was not certified by peer review) is the author/funder, who has granted bioRxiv a license to display the preprint in perpetuity. It is made available under aCC-BY-NC-ND 4.0 International license.

all infection differentially-expressed genes in at least one cell type. To obtain p-values for the ranked list of specificity scores, we used GOrilla (Eden et al., 2009). Notably, GOrilla relies on a statistical framework (the minimum hypergeometric score) that allows the calculation of exact p-values for observed enrichments in ranked lists of genes, taking into account multiple testing without needing to perform simulations, unlike fgsea. Because GOrilla only identifies GO terms that are significantly enriched at the top of the ranked gene list, we performed the enrichments in two ways, once with the list ranked from high to low specificity scores and again with the list ranked from low to high specificity scores. The Benjamini-Hochberg adjusted FDR q-values calculated by GOrilla for the "viral gene expression" and "response to type I interferon" terms are reported in Fig. 1G.

We performed gene set enrichment analysis for our intersection set of popDE genes and eGenes (Fig. 3E) using the ClueGO (v2.5.7) (Bindea et al., 2009) Cytoscape (v3.7.1) (Shannon et al., 2003) module in functional analysis mode, where the target set of genes was the list of popDE eGenes in the mock or IAV condition and the background set was the list of genes tested across all cell types. Specifically, we tested for the enrichment of GO terms related to biological processes (ontology source: GO_BiologicalProcess-EBI-UniProt-GOA_04.09.2018_00h00) using the following parameters: visual style = Groups, default Network Specificity, no GO Term Fusion, min. GO Tree Interval level = 3, max. GO Tree Interval level = 8, min. number of genes = 3, min. percentage of genes = 4.0, statistical test used = Enrichment/Depletion (two-sided hypergeometric test), p-value correction = Benjamini-Hochberg. For the graphical representation of the enrichment analysis, ClueGO clustering functionality was used (kappa threshold score for considering or rejecting term-to-term links set to 0.4). Only pathways with an FDR < 0.01 are reported.

bioRxiv preprint doi: https://doi.org/10.1101/2020.12.21.423830; this version posted December 21, 2020. The copyright holder for this preprint (which was not certified by peer review) is the author/funder, who has granted bioRxiv a license to display the preprint in perpetuity. It is made available under aCC-BY-NC-ND 4.0 International license.

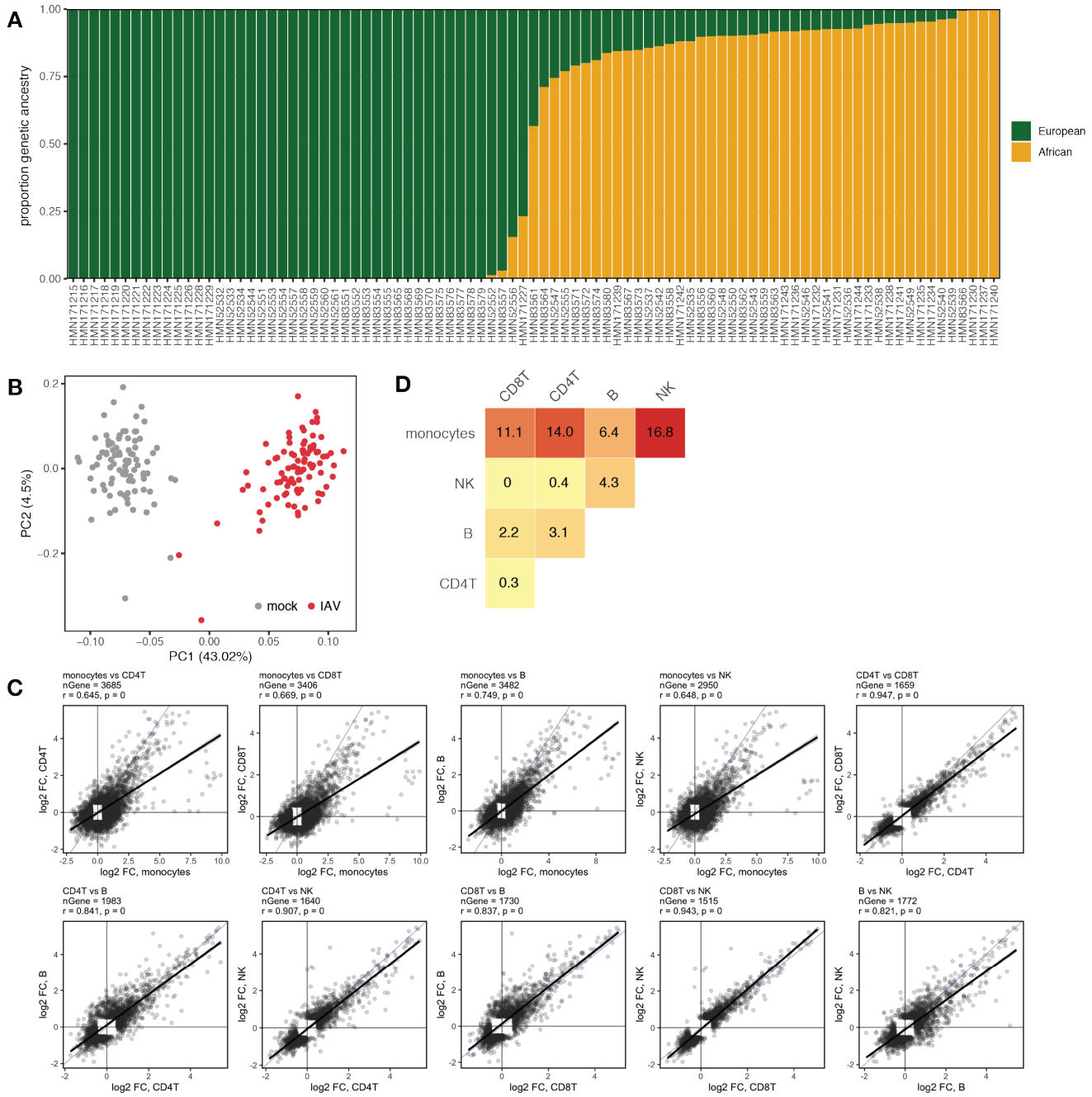

Fig. S1. Overview of samples and global infection effects. (A) Quantitative genetic ancestry proportions partitioned into European (green) and African (yellow) components for each individual. (B) PCA decomposition of the pseudobulk PBMC expression data in mock-exposed (grey) and IAV-infected (red) samples. PC1 (percent variance explained = 43.02%) separates samples by infection status. (C) Pairwise effect size correlations across cell types among genes

bioRxiv preprint doi: https://doi.org/10.1101/2020.12.21.423830; this version posted December 21, 2020. The copyright holder for this preprint (which was not certified by peer review) is the author/funder, who has granted bioRxiv a license to display the preprint in perpetuity. It is made available under aCC-BY-NC-ND 4.0 International license.

that are DE (logFC > 0.5, FDR < 0.05) upon IAV infection in either of the cell types being compared. (D) Pairwise comparisons of the percentage of DE genes in both cell types being compared that show discordant effect sizes.

bioRxiv preprint doi: https://doi.org/10.1101/2020.12.21.423830; this version posted December 21, 2020. The copyright holder for this preprint (which was not certified by peer review) is the author/funder, who has granted bioRxiv a license to display the preprint in perpetuity. It is made available under aCC-BY-NC-ND 4.0 International license.

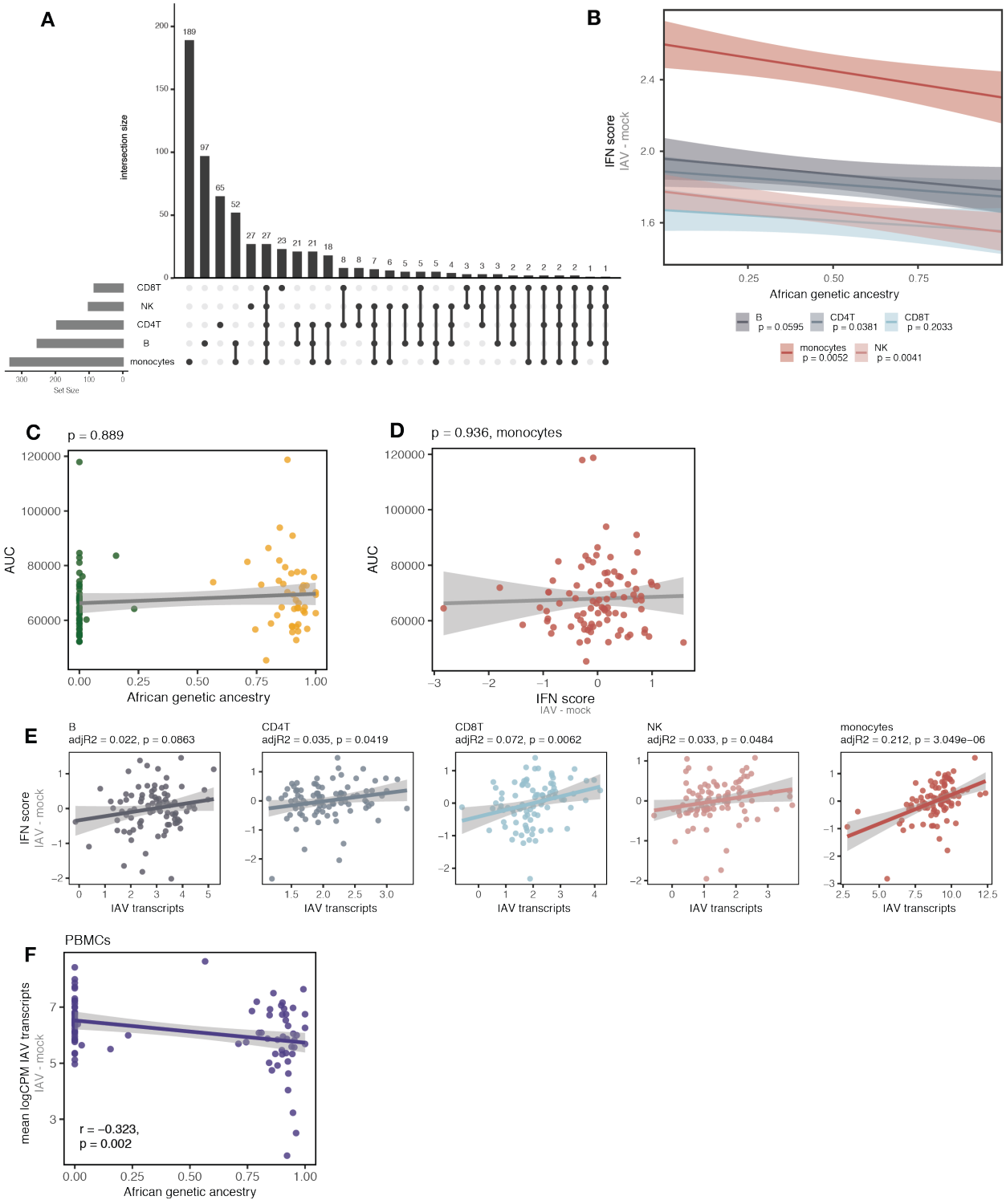

Fig. S2. Population-associated responses to IAV infection. (A) Sharing of significant popDR genes (lfsr < 0.10) across cell types. (B) Correlation between the proportion of African genetic ancestry (x-axis) and IFN score response (y-axis) across individuals (mean Pearson's r across

bioRxiv preprint doi: https://doi.org/10.1101/2020.12.21.423830; this version posted December 21, 2020. The copyright holder for this preprint (which was not certified by peer review) is the author/funder, who has granted bioRxiv a license to display the preprint in perpetuity. It is made available under aCC-BY-NC-ND 4.0 International license.

cell types = -0.23, Fisher's meta-p = $6x10^{-5}$). (C) Correlation between the proportion of African genetic ancestry (x-axis) and baseline levels of IAV-specific serum IgG antibodies. We quantified anti-A/Cal/04/09 antibody titers using 4-fold serial dilutions for each individual's serum and a total of eight dilutions per sample. We then used the dilution and absorbances to generate an area under the curve (AUC; y-axis), which we used to summarize the levels of IAV (A/Cal/04/09)-specific serum IgG antibodies detected in each individual. (D) Correlation between IFN score response (x-axis) and baseline levels of IAV-specific serum IgG antibodies ("AUC" = area under the curve, y-axis). (E) Correlation between IAV transcript expression (x-axis) and the IFN response (y-axis) across individuals within each cell type. Higher IAV transcript expression is significantly associated with a stronger IFN response in $CD4^+$ T cells, $CD8^+$ T cells, monocytes, and NK cells ($p < 0.05$), with monocytes showing the strongest correlation (adj $R^2 = 0.212$, $p = 3.1x10^{-6}$). (F) African genetic ancestry is significantly negatively correlated with IAV transcript expression (Pearson's $r = -0.323$, $p = 0.002$) in PBMCs. In (B), (C), (D), (E) and (F) lines show the best-fit slope and intercept from linear models for cell types shown.

bioRxiv preprint doi: https://doi.org/10.1101/2020.12.21.423830; this version posted December 21, 2020. The copyright holder for this preprint (which was not certified by peer review) is the author/funder, who has granted bioRxiv a license to display the preprint in perpetuity. It is made available under aCC-BY-NC-ND 4.0 International license.

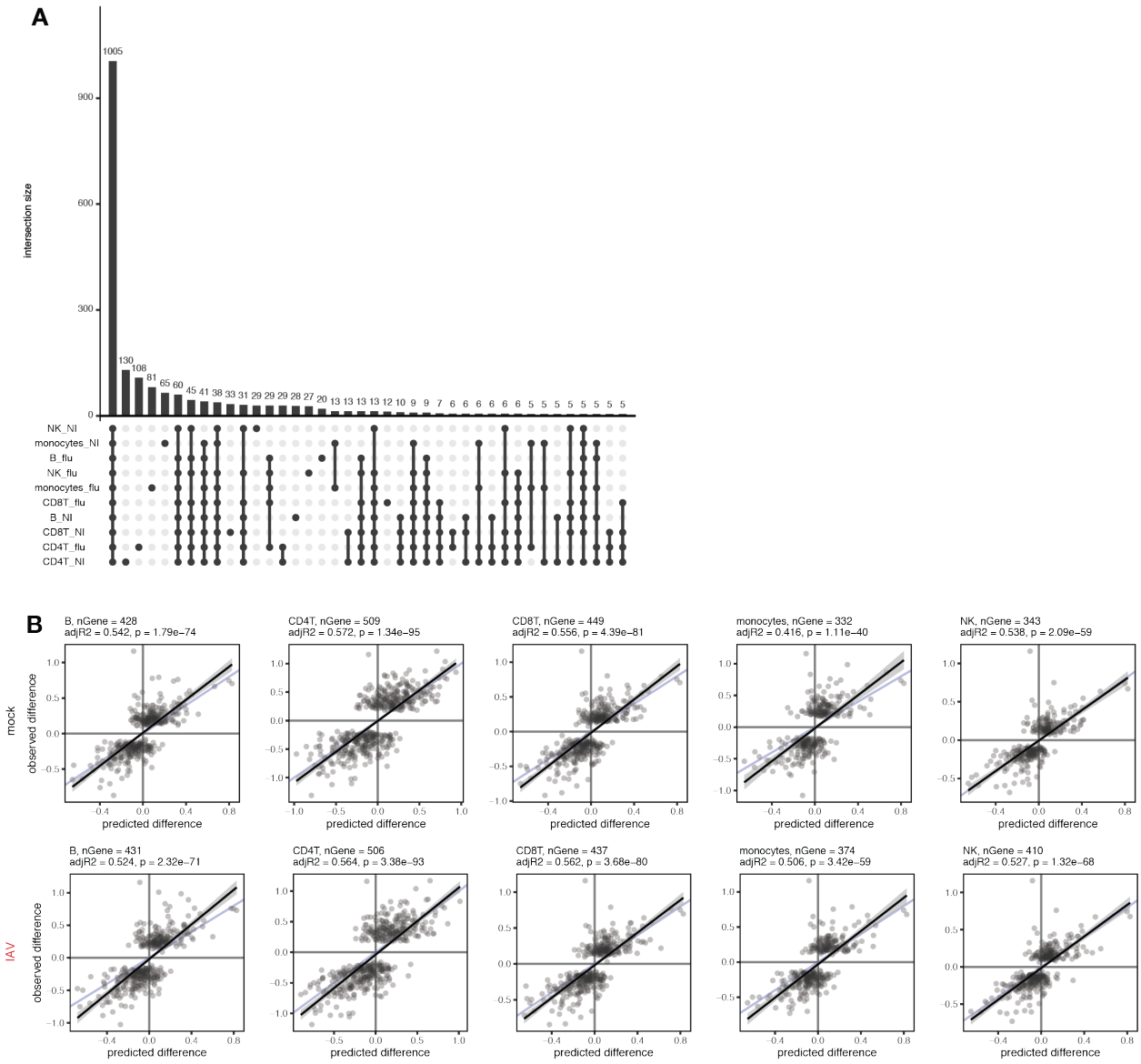

Fig. S3. *Cis*-genetic effects regulate gene expression. (A) Sharing of significant eGenes (lfsr < 0.10) across cell types and treatment conditions. (B) Correlation of the *cis*-predicted population differences in expression (x-axis) versus the observed population differences in expression (y-axis) among popDE genes with an eQTL across all cell types in the mock-exposed condition (top) and IAV-infected condition (bottom). The black line shows the best-fit line from a linear model, and the blue line shows the identity (1:1) line.

bioRxiv preprint doi: https://doi.org/10.1101/2020.12.21.423830; this version posted December 21, 2020. The copyright holder for this preprint (which was not certified by peer review) is the author/funder, who has granted bioRxiv a license to display the preprint in perpetuity. It is made available under aCC-BY-NC-ND 4.0 International license.

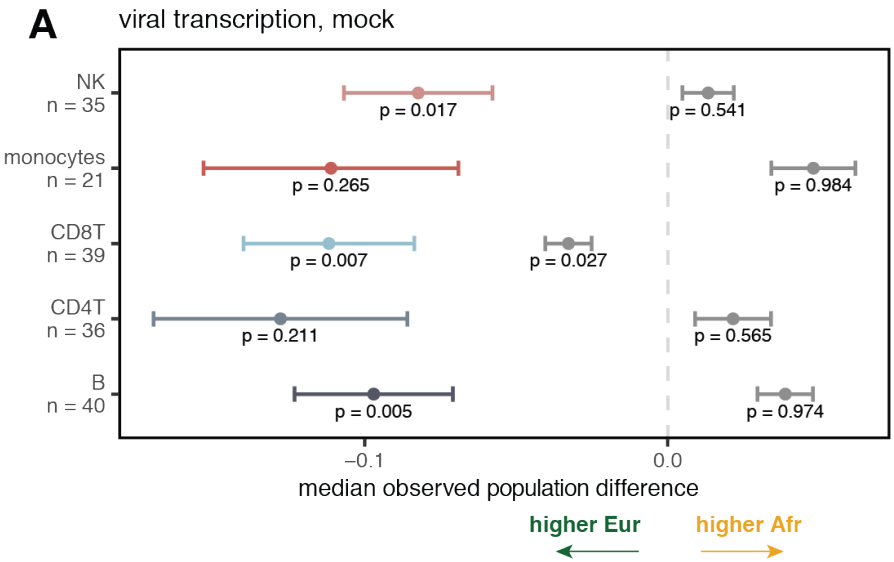

Fig. S4. Impact of *cis*-regression on population-associated expression differences. (A) Example term showing the effect of *cis*-SNP regression. In the mock condition, EA individuals display higher expression (median observed pop. difference < 0, colored point +/- SE) of the genes belonging to the "viral transcription" term in the observed data. *Cis*-SNP regression (grey bars) reduces this effect. Points represent the median value +/- SE.

bioRxiv preprint doi: https://doi.org/10.1101/2020.12.21.423830; this version posted December 21, 2020. The copyright holder for this preprint (which was not certified by peer review) is the author/funder, who has granted bioRxiv a license to display the preprint in perpetuity. It is made available under aCC-BY-NC-ND 4.0 International license.

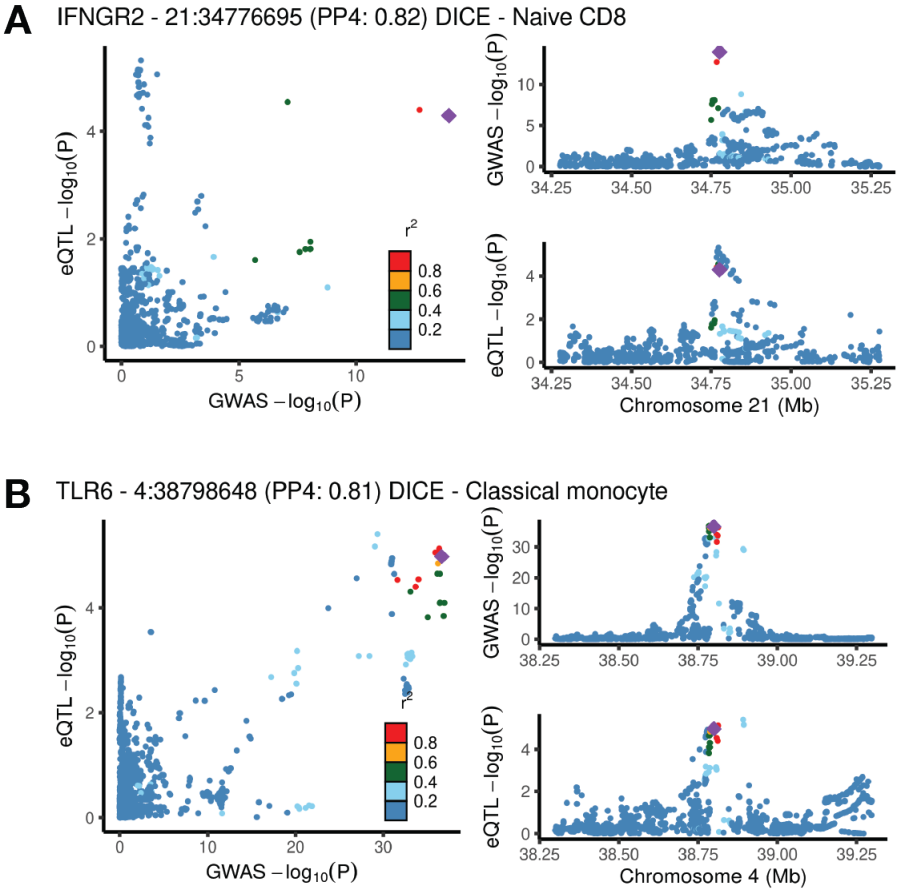

Fig. S5. Colocalization signals. (A) *IFNGR2* colocalizes with rs2284553 in naïve CD8$^+$ T cells in the Crohn's disease GWAS (de Lange et al.). (B) *TLR6* colocalizes with rs5743618 in classical monocytes in the allergic disease GWAS. For both (A) and (B), the plot on the left shows the correlation between GWAS p-values (x-axis) and eQTL p-values (y-axis). Plots on the right show the Manhattan plots for the GWAS signal (top) and the eQTL signal (bottom).

bioRxiv preprint doi: https://doi.org/10.1101/2020.12.21.423830; this version posted December 21, 2020. The copyright holder for this preprint (which was not certified by peer review) is the author/funder, who has granted bioRxiv a license to display the preprint in perpetuity. It is made available under aCC-BY-NC-ND 4.0 International license.

1093 **Table S11.** Principal components (PCs) regressed in the eQTL analysis.

Cell type	Regressed PCs (mock)	Regressed PCs (IAV)	No. genes under 0.10 FDR (mock)	No. genes under 0.10 FDR (IAV)
$CD4^+$ T	1 to 4	1 to 2	1377	1176
B	1 to 6	1 to 3	152	196
NK	1 to 2	1 to 2	68	76
monocytes	1 to 10	1 to 7	265	251
$CD8^+$ T	1 to 6	1 to 4	204	178
PBMC	1 to 6	1 to 3	2095	1809

1094

1095

bioRxiv preprint doi: https://doi.org/10.1101/2020.12.21.423830; this version posted December 21, 2020. The copyright holder for this preprint (which was not certified by peer review) is the author/funder, who has granted bioRxiv a license to display the preprint in perpetuity. It is made available under aCC-BY-NC-ND 4.0 International license.

References

Abubakar, I., Myhill, D., Aliyu, S.H., and Hunter, P.R. (2008). Detection of Mycobacterium avium subspecies paratuberculosis from patients with Crohn's disease using nucleic acid-based techniques: a systematic review and meta-analysis. Inflamm Bowel Dis *14*, 401–410.

Albright, F.S., Orlando, P., Pavia, A.T., Jackson, G.G., and Cannon Albright, L.A. (2008). Evidence for a heritable predisposition to death due to influenza. J Infect Dis *197*, 18–24.

Alexander, D.H., and Lange, K. (2011). Enhancements to the ADMIXTURE algorithm for individual ancestry estimation. BMC Bioinformatics *12*, 246.

Auton, A., Abecasis, G.R., Altshuler, D.M., Durbin, R.M., Abecasis, G.R., Bentley, D.R., Chakravarti, A., Clark, A.G., Donnelly, P., Eichler, E.E., et al. (2015). A global reference for human genetic variation. Nature *526*, 68–74.

Barreiro, L.B., Ben-Ali, M., Quach, H., Laval, G., Patin, E., Pickrell, J.K., Bouchier, C., Tichit, M., Neyrolles, O., Gicquel, B., et al. (2009). Evolutionary Dynamics of Human Toll-Like Receptors and Their Different Contributions to Host Defense. PLOS Genet *5*, e1000562.

Barreiro, L.B., Tailleux, L., Pai, A.A., Gicquel, B., Marioni, J.C., and Gilad, Y. (2012). Deciphering the genetic architecture of variation in the immune response to Mycobacterium tuberculosis infection. PNAS *109*, 1204–1209.

Battle, A., Mostafavi, S., Zhu, X., Potash, J.B., Weissman, M.M., McCormick, C., Haudenschild, C.D., Beckman, K.B., Shi, J., Mei, R., et al. (2014). Characterizing the genetic basis of transcriptome diversity through RNA-sequencing of 922 individuals. Genome Res. *24*, 14–24.

Bianco, C., and Mohr, I. (2019). Ribosome biogenesis restricts innate immune responses to virus infection and DNA. ELife *8*, e49551.

Bickel, M. (1993). The role of interleukin-8 in inflammation and mechanisms of regulation. J Periodontol *64*, 456–460.

Bindea, G., Mlecnik, B., Hackl, H., Charoentong, P., Tosolini, M., Kirilovsky, A., Fridman, W.-H., Pagès, F., Trajanoski, Z., and Galon, J. (2009). ClueGO: a Cytoscape plug-in to decipher functionally grouped gene ontology and pathway annotation networks. Bioinformatics *25*, 1091–1093.

Bonnevie-Nielsen, V., Field, L.L., Lu, S., Zheng, D.-J., Li, M., Martensen, P.M., Nielsen, T.B., Beck-Nielsen, H., Lau, Y.-L., and Pociot, F. (2005). Variation in antiviral 2',5'-oligoadenylate synthetase (2'5'AS) enzyme activity is controlled by a single-nucleotide polymorphism at a splice-acceptor site in the OAS1 gene. Am J Hum Genet *76*, 623–633.

Brinkworth, J.F., and Barreiro, L.B. (2014). The contribution of natural selection to present-day susceptibility to chronic inflammatory and autoimmune disease. Curr Opin Immunol *31*, 66–78.

Bustamante, C.D., Burchard, E.G., and De la Vega, F.M. (2011). Genomics for the world. Nature *475*, 163–165.

bioRxiv preprint doi: https://doi.org/10.1101/2020.12.21.423830; this version posted December 21, 2020. The copyright holder for this preprint (which was not certified by peer review) is the author/funder, who has granted bioRxiv a license to display the preprint in perpetuity. It is made available under aCC-BY-NC-ND 4.0 International license.

1132 Ca, D., and Sh, K. (2006). IL-32, a novel cytokine with a possible role in disease (Ann Rheum
1133 Dis).

1134 CDC (2020). Racial and Ethnic Minority Groups.

1135 Chang, C.C., Chow, C.C., Tellier, L.C., Vattikuti, S., Purcell, S.M., and Lee, J.J. (2015). Second-
1136 generation PLINK: rising to the challenge of larger and richer datasets. Gigascience *4*, 7.

1137 Chen, L., Ge, B., Casale, F.P., Vasquez, L., Kwan, T., Garrido-Martín, D., Watt, S., Yan, Y.,
1138 Kundu, K., Ecker, S., et al. (2016). Genetic Drivers of Epigenetic and Transcriptional Variation in
1139 Human Immune Cells. Cell *167*, 1398-1414.e24.

1140 Danecek, P., Auton, A., Abecasis, G., Albers, C.A., Banks, E., DePristo, M.A., Handsaker, R.E.,
1141 Lunter, G., Marth, G.T., Sherry, S.T., et al. (2011). The variant call format and VCFtools.
1142 Bioinformatics *27*, 2156–2158.

1143 Eden, E., Navon, R., Steinfeld, I., Lipson, D., and Yakhini, Z. (2009). GOrilla: a tool for discovery
1144 and visualization of enriched GO terms in ranked gene lists. BMC Bioinformatics *10*, 48.

1145 El Awady, M.K., Anany, M.A., Esmat, G., Zayed, N., Tabll, A.A., Helmy, A., El Zayady, A.R.,
1146 Abdalla, M.S., Sharada, H.M., El Raziky, M., et al. (2011). Single nucleotide polymorphism at
1147 exon 7 splice acceptor site of OAS1 gene determines response of hepatitis C virus patients to
1148 interferon therapy. J Gastroenterol Hepatol *26*, 843–850.

1149 Enard, D., and Petrov, D.A. (2018). Evidence that RNA Viruses Drove Adaptive Introgression
1150 between Neanderthals and Modern Humans. Cell *175*, 360-371.e13.

1151 Enard, D., and Petrov, D.A. (2020). Ancient RNA virus epidemics through the lens of recent
1152 adaptation in human genomes. Philosophical Transactions of the Royal Society B: Biological
1153 Sciences *375*, 20190575.

1154 Enard, D., Cai, L., Gwennap, C., and Petrov, D.A. (2016). Viruses are a dominant driver of protein
1155 adaptation in mammals. ELife *5*, e12469.

1156 Fairfax, B.P., Humburg, P., Makino, S., Naranbhai, V., Wong, D., Lau, E., Jostins, L., Plant, K.,
1157 Andrews, R., McGee, C., et al. (2014). Innate Immune Activity Conditions the Effect of Regulatory
1158 Variants upon Monocyte Gene Expression. Science *343*, 1246949.

1159 Feller, M., Huwiler, K., Stephan, R., Altpeter, E., Shang, A., Furrer, H., Pfyffer, G.E., Jemmi, T.,
1160 Baumgartner, A., and Egger, M. (2007). Mycobacterium avium subspecies paratuberculosis and
1161 Crohn's disease: a systematic review and meta-analysis. Lancet Infect Dis *7*, 607–613.

1162 Fodor, E., Devenish, L., Engelhardt, O.G., Palese, P., Brownlee, G.G., and García-Sastre, A.
1163 (1999). Rescue of Influenza A Virus from Recombinant DNA. J Virol *73*, 9679–9682.

1164 Fromont-Racine, M., Senger, B., Saveanu, C., and Fasiolo, F. (2003). Ribosome assembly in
1165 eukaryotes. Gene *313*, 17–42.

1166 Fumagalli, M., Sironi, M., Pozzoli, U., Ferrer-Admettla, A., Pattini, L., and Nielsen, R. (2011).
1167 Signatures of Environmental Genetic Adaptation Pinpoint Pathogens as the Main Selective
1168 Pressure through Human Evolution. PLOS Genetics *7*, e1002355.

bioRxiv preprint doi: https://doi.org/10.1101/2020.12.21.423830; this version posted December 21, 2020. The copyright holder for this preprint (which was not certified by peer review) is the author/funder, who has granted bioRxiv a license to display the preprint in perpetuity. It is made available under aCC-BY-NC-ND 4.0 International license.

1169 Giambartolomei, C., Vukcevic, D., Schadt, E.E., Franke, L., Hingorani, A.D., Wallace, C., and
1170 Plagnol, V. (2014). Bayesian Test for Colocalisation between Pairs of Genetic Association Studies
1171 Using Summary Statistics. PLOS Genetics *10*, e1004383.

1172 Gymrek, M., Willems, T., Guilmatre, A., Zeng, H., Markus, B., Georgiev, S., Daly, M.J., Price, A.L.,
1173 Pritchard, J.K., Sharp, A.J., et al. (2016). Abundant contribution of short tandem repeats to gene
1174 expression variation in humans. Nat Genet *48*, 22–29.

1175 Hai, R., Schmolke, M., Varga, Z.T., Manicassamy, B., Wang, T.T., Belser, J.A., Pearce, M.B.,
1176 García-Sastre, A., Tumpey, T.M., and Palese, P. (2010). PB1-F2 Expression by the 2009
1177 Pandemic H1N1 Influenza Virus Has Minimal Impact on Virulence in Animal Models. Journal of
1178 Virology *84*, 4442–4450.

1179 Haque, A., and Mir, M.A. (2010). Interaction of Hantavirus Nucleocapsid Protein with Ribosomal
1180 Protein S19. J Virol *84*, 12450–12453.

1181 Heaton, H., Talman, A.M., Knights, A., Imaz, M., Gaffney, D.J., Durbin, R., Hemberg, M., and
1182 Lawniczak, M.K.N. (2020). Souporcell: robust clustering of single-cell RNA-seq data by genotype
1183 without reference genotypes. Nature Methods *17*, 615–620.

1184 Herrero, J., Muffato, M., Beal, K., Fitzgerald, S., Gordon, L., Pignatelli, M., Vilella, A.J., Searle,
1185 S.M.J., Amode, R., Brent, S., et al. (2016). Ensembl comparative genomics resources. Database
1186 (Oxford) *2016*.

1187 Hoffmann, E., Neumann, G., Kawaoka, Y., Hobom, G., and Webster, R.G. (2000). A DNA
1188 transfection system for generation of influenza A virus from eight plasmids. PNAS *97*, 6108–6113.

1189 Huang, J.-Y., Su, W.-C., Jeng, K.-S., Chang, T.-H., and Lai, M.M.C. (2012). Attenuation of 40S
1190 Ribosomal Subunit Abundance Differentially Affects Host and HCV Translation and Suppresses
1191 HCV Replication. PLoS Pathog *8*.

1192 James, J.A., Neas, B.R., Moser, K.L., Hall, T., Bruner, G.R., Sestak, A.L., and Harley, J.B. (2001).
1193 Systemic lupus erythematosus in adults is associated with previous Epstein-Barr virus exposure.
1194 Arthritis Rheum *44*, 1122–1126.

1195 Kang, S., Brown, H.M., and Hwang, S. (2018). Direct Antiviral Mechanisms of Interferon-Gamma.
1196 Immune Netw *18*.

1197 Kelley-Hedgepeth, A., Lloyd-Jones, D.M., Colvin, A., Matthews, K.A., Johnston, J., Sowers, M.R.,
1198 Sternfeld, B., Pasternak, R.C., Chae, C.U., and SWAN Investigators (2008). Ethnic differences in
1199 C-reactive protein concentrations. Clin Chem *54*, 1027–1037.

1200 Kenney, A.D., Dowdle, J.A., Bozzacco, L., McMichael, T.M., St Gelais, C., Panfil, A.R., Sun, Y.,
1201 Schlesinger, L.S., Anderson, M.Z., Green, P.L., et al. (2017). Human Genetic Determinants of
1202 Viral Diseases. Annu Rev Genet *51*, 241–263.

1203 Korotkevich, G., Sukhov, V., and Sergushichev, A. (2019). Fast gene set enrichment analysis.
1204 BioRxiv 060012.

bioRxiv preprint doi: https://doi.org/10.1101/2020.12.21.423830; this version posted December 21, 2020. The copyright holder for this preprint (which was not certified by peer review) is the author/funder, who has granted bioRxiv a license to display the preprint in perpetuity. It is made available under aCC-BY-NC-ND 4.0 International license.

Kwon, Y.-C., Kang, J.-I., Hwang, S.B., and Ahn, B.-Y. (2013). The ribonuclease L-dependent antiviral roles of human 2',5'-oligoadenylate synthetase family members against hepatitis C virus. FEBS Lett *587*, 156–164.

Lappalainen, T., Sammeth, M., Friedländer, M.R., 't Hoen, P.A.C., Monlong, J., Rivas, M.A., Gonzàlez-Porta, M., Kurbatova, N., Griebel, T., Ferreira, P.G., et al. (2013). Transcriptome and genome sequencing uncovers functional variation in humans. Nature *501*, 506–511.

Lee, M.N., Ye, C., Villani, A.-C., Raj, T., Li, W., Eisenhaure, T.M., Imboywa, S.H., Chipendo, P.I., Ran, F.A., Slowikowski, K., et al. (2014). Common Genetic Variants Modulate Pathogen-Sensing Responses in Human Dendritic Cells. Science *343*.

Li, H. (2011). A statistical framework for SNP calling, mutation discovery, association mapping and population genetical parameter estimation from sequencing data. Bioinformatics *27*, 2987–2993.

Li, S. (2019). Regulation of Ribosomal Proteins on Viral Infection. Cells *8*.

Liberzon, A., Birger, C., Thorvaldsdóttir, H., Ghandi, M., Mesirov, J.P., and Tamayo, P. (2015). The Molecular Signatures Database Hallmark Gene Set Collection. Cels *1*, 417–425.

Lim, J.K., Lisco, A., McDermott, D.H., Huynh, L., Ward, J.M., Johnson, B., Johnson, H., Pape, J., Foster, G.A., Krysztof, D., et al. (2009). Genetic variation in OAS1 is a risk factor for initial infection with West Nile virus in man. PLoS Pathog *5*, e1000321.

Maclean, C.A., Chue Hong, N.P., and Prendergast, J.G.D. (2015). hapbin: An Efficient Program for Performing Haplotype-Based Scans for Positive Selection in Large Genomic Datasets. Mol Biol Evol *32*, 3027–3029.

Mu, Z., Wei, W., Fair, B., Miao, J., Zhu, P., and Li, Y.I. (2020). Impact of cell-type and context-dependent regulatory variants on human immune traits. BioRxiv 2020.07.20.212753.

Nédélec, Y., Sanz, J., Baharian, G., Szpiech, Z.A., Pacis, A., Dumaine, A., Grenier, J.-C., Freiman, A., Sams, A.J., Hebert, S., et al. (2016). Genetic Ancestry and Natural Selection Drive Population Differences in Immune Responses to Pathogens. Cell *167*, 657-669.e21.

Nielsen, R., Akey, J.M., Jakobsson, M., Pritchard, J.K., Tishkoff, S., and Willerslev, E. (2017). Tracing the peopling of the world through genomics. Nature *541*, 302–310.

O'Neill, M., Quach, H., Pothlichet, J., Aquino, Y., Bisiaux, A., Zidane, N., Deschamps, M., Libri, V., Hasan, M., Zhang, S.-Y., et al. (2020). Basal Expression of Interferon-Stimulated Genes Drives Population Differences in Monocyte Susceptibility to Influenza Infection. BioRxiv 2020.12.07.414151.

Pennington, R., Gatenbee, C., Kennedy, B., Harpending, H., and Cochran, G. (2009). Group differences in proneness to inflammation. Infection, Genetics and Evolution *9*, 1371–1380.

Piasecka, B., Duffy, D., Urrutia, A., Quach, H., Patin, E., Posseme, C., Bergstedt, J., Charbit, B., Rouilly, V., MacPherson, C.R., et al. (2018). Distinctive roles of age, sex, and genetics in shaping transcriptional variation of human immune responses to microbial challenges. PNAS *115*, E488–E497.

bioRxiv preprint doi: https://doi.org/10.1101/2020.12.21.423830; this version posted December 21, 2020. The copyright holder for this preprint (which was not certified by peer review) is the author/funder, who has granted bioRxiv a license to display the preprint in perpetuity. It is made available under aCC-BY-NC-ND 4.0 International license.

1243 Quach, H., and Quintana-Murci, L. (2017). Living in an adaptive world: Genomic dissection of the
1244 genus Homo and its immune response. Journal of Experimental Medicine *214*, 877–894.

1245 Quach, H., Rotival, M., Pothlichet, J., Loh, Y.-H.E., Dannemann, M., Zidane, N., Laval, G., Patin,
1246 E., Harmant, C., Lopez, M., et al. (2016). Genetic Adaptation and Neandertal Admixture Shaped
1247 the Immune System of Human Populations. Cell *167*, 643-656.e17.

1248 Ramos-Casals, M., Jara, L.-J., Medina, F., Rosas, J., Calvo-Alen, J., Mañá, J., Anaya, J.-M., Font,
1249 J., and HISPAMEC Study Group (2005). Systemic autoimmune diseases co-existing with chronic
1250 hepatitis C virus infection (the HISPAMEC Registry): patterns of clinical and immunological
1251 expression in 180 cases. J Intern Med *257*, 549–557.

1252 Ritchie, M.E., Phipson, B., Wu, D., Hu, Y., Law, C.W., Shi, W., and Smyth, G.K. (2015). limma
1253 powers differential expression analyses for RNA-sequencing and microarray studies. Nucleic
1254 Acids Res *43*, e47–e47.

1255 Robinson, M.D., McCarthy, D.J., and Smyth, G.K. (2010). edgeR: a Bioconductor package for
1256 differential expression analysis of digital gene expression data. Bioinformatics *26*, 139–140.

1257 Saebo, A., Vik, E., Lange, O.J., and Matuszkiewicz, L. (2005). Inflammatory bowel disease
1258 associated with Yersinia enterocolitica O:3 infection. European Journal of Internal Medicine *16*,
1259 176–182.

1260 Sams, A.J., Dumaine, A., Nédélec, Y., Yotova, V., Alfieri, C., Tanner, J.E., Messer, P.W., and
1261 Barreiro, L.B. (2016). Adaptively introgressed Neandertal haplotype at the OAS locus functionally
1262 impacts innate immune responses in humans. Genome Biology *17*, 246.

1263 Sanz, J., Randolph, H.E., and Barreiro, L.B. (2018). Genetic and evolutionary determinants of
1264 human population variation in immune responses. Current Opinion in Genetics & Development
1265 *53*, 28–35.

1266 Schmiedel, B.J., Singh, D., Madrigal, A., Valdovino-Gonzalez, A.G., White, B.M., Zapardiel-
1267 Gonzalo, J., Ha, B., Altay, G., Greenbaum, J.A., McVicker, G., et al. (2018). Impact of Genetic
1268 Polymorphisms on Human Immune Cell Gene Expression. Cell *175*, 1701-1715.e16.

1269 Shabalin, A.A. (2012). Matrix eQTL: ultra fast eQTL analysis via large matrix operations.
1270 Bioinformatics *28*, 1353–1358.

1271 Shannon, P., Markiel, A., Ozier, O., Baliga, N.S., Wang, J.T., Ramage, D., Amin, N., Schwikowski,
1272 B., and Ideker, T. (2003). Cytoscape: A Software Environment for Integrated Models of
1273 Biomolecular Interaction Networks. Genome Res *13*, 2498–2504.

1274 Siddle, K.J., and Quintana-Murci, L. (2014). The Red Queen's long race: human adaptation to
1275 pathogen pressure. Curr Opin Genet Dev *29*, 31–38.

1276 Snyder-Mackler, N., Sanz, J., Kohn, J.N., Brinkworth, J.F., Morrow, S., Shaver, A.O., Grenier, J.-
1277 C., Pique-Regi, R., Johnson, Z.P., Wilson, M.E., et al. (2016). Social status alters immune
1278 regulation and response to infection in macaques. Science *354*, 1041–1045.

1279 Storey, J.D., and Tibshirani, R. (2003). Statistical significance for genomewide studies. PNAS
1280 *100*, 9440–9445.

bioRxiv preprint doi: https://doi.org/10.1101/2020.12.21.423830; this version posted December 21, 2020. The copyright holder for this preprint (which was not certified by peer review) is the author/funder, who has granted bioRxiv a license to display the preprint in perpetuity. It is made available under aCC-BY-NC-ND 4.0 International license.

1281 Stuart, T., Butler, A., Hoffman, P., Hafemeister, C., Papalexi, E., Mauck, W.M., Hao, Y., Stoeckius,
1282 M., Smibert, P., and Satija, R. (2019). Comprehensive Integration of Single-Cell Data. Cell *177*,
1283 1888-1902.e21.

1284 Subramanian, A., Tamayo, P., Mootha, V.K., Mukherjee, S., Ebert, B.L., Gillette, M.A., Paulovich,
1285 A., Pomeroy, S.L., Golub, T.R., Lander, E.S., et al. (2005). Gene set enrichment analysis: a
1286 knowledge-based approach for interpreting genome-wide expression profiles. Proc Natl Acad Sci
1287 U S A *102*, 15545–15550.

1288 Urbut, S.M., Wang, G., Carbonetto, P., and Stephens, M. (2019). Flexible statistical methods for
1289 estimating and testing effects in genomic studies with multiple conditions. Nat Genet *51*, 187–
1290 195.

1291 Vabret, N., Britton, G.J., Gruber, C., Hegde, S., Kim, J., Kuksin, M., Levantovsky, R., Malle, L.,
1292 Moreira, A., Park, M.D., et al. (2020). Immunology of COVID-19: Current State of the Science.
1293 Immunity *52*, 910–941.

1294 Voight, B.F., Kudaravalli, S., Wen, X., and Pritchard, J.K. (2006). A Map of Recent Positive
1295 Selection in the Human Genome. PLOS Biology *4*, e72.

1296 Vyas, K., Chaudhuri, S., Leaman, D.W., Komar, A.A., Musiyenko, A., Barik, S., and Mazumder,
1297 B. (2009). Genome-Wide Polysome Profiling Reveals an Inflammation-Responsive
1298 Posttranscriptional Operon in Gamma Interferon-Activated Monocytes. Mol Cell Biol *29*, 458–470.

1299 Wallace, C. (2020). Eliciting priors and relaxing the single causal variant assumption in
1300 colocalisation analyses. PLOS Genetics *16*, e1008720.

1301 Wan, F., Weaver, A., Gao, X., Bern, M., Hardwidge, P.R., and Lenardo, M.J. (2011). IKKβ
1302 phosphorylation regulates RPS3 nuclear translocation and NF-κB function during Escherichia coli
1303 O157:H7 infection. Nat Immunol *12*, 335–343.

1304 Wei, J., and Yewdell, J.W. (2019). Immunoribosomes: Where's there's fire, there's fire. Molecular
1305 Immunology *113*, 38–42.

1306 Weir, B.S., and Cockerham, C.C. (1984). Estimating F-Statistics for the Analysis of Population
1307 Structure. Evolution *38*, 1358–1370.

1308 Yamazaki, M., Kitamura, R., Kusano, S., Eda, H., Sato, S., Okawa-Takatsuji, M., Aotsuka, S., and
1309 Yanagi, K. (2005). Elevated immunoglobulin G antibodies to the proline-rich amino-terminal
1310 region of Epstein-Barr virus nuclear antigen-2 in sera from patients with systemic connective
1311 tissue diseases and from a subgroup of Sjögren's syndrome patients with pulmonary
1312 involvements. Clin Exp Immunol *139*, 558–568.

1313 Yan, H., He, D., Huang, X., Zhang, E., Chen, Q., Xu, R., Liu, X., Zi, F., and Cai, Z. (2018). Role
1314 of interleukin-32 in cancer biology. Oncol Lett *16*, 41–47.

1315 Yewdell, J.W. (2007). Plumbing the sources of endogenous MHC class I peptide ligands. Current
1316 Opinion in Immunology *19*, 79–86.

1317 Zhao, H., Sun, Z., Wang, J., Huang, H., Kocher, J.-P., and Wang, L. (2014). CrossMap: a versatile
1318 tool for coordinate conversion between genome assemblies. Bioinformatics *30*, 1006–1007.

bioRxiv preprint doi: https://doi.org/10.1101/2020.12.21.423830; this version posted December 21, 2020. The copyright holder for this preprint (which was not certified by peer review) is the author/funder, who has granted bioRxiv a license to display the preprint in perpetuity. It is made available under aCC-BY-NC-ND 4.0 International license.

1319 Zheng, X., Levine, D., Shen, J., Gogarten, S.M., Laurie, C., and Weir, B.S. (2012). A high-
1320 performance computing toolset for relatedness and principal component analysis of SNP data.
1321 Bioinformatics *28*, 3326–3328.

1322